remote sensing

MDPI

Article

Exploring Spatio-Temporal Dynamics of Future Extreme Precipitation, Runoff, and Flood Risk in the Hanjiang River Basin, China

Dong Wang [1,2], Weiwei Shao [3], Jiahong Liu [3,*], Hui Su [1,2], Ga Zhang [4] and Xiaoran Fu [5]

[1] School of Water Conservancy and Hydroelectric Power, Hebei University of Engineering, Handan 056038, China; wangdong8@hebeu.edu.cn (D.W.); suh-26@163.com (H.S.)
[2] Hebei Key Laboratory of Intelligent Water Conservancy, Hebei University of Engineering, Handan 056038, China
[3] State Key Laboratory of Simulation and Regulation of Water Cycle in River Basin, China Institute of Water Resources and Hydropower Research, Beijing 100038, China; shaoww@iwhr.com
[4] State Key Laboratory of Hydroscience and Engineering, Tsinghua University, Beijing 100084, China; zhangga18@mails.tsinghua.edu.cn
[5] National Institute of Natural Hazards, Ministry of Emergency Management of China, Beijing 100085, China; xiaoranfu@ninhm.ac.cn
* Correspondence: liujh@iwhr.com

Abstract: The hydrological cycle is altered by climate change and human activities, amplifying extreme precipitation and heightening the flood risk regionally and globally. It is imperative to explore the future possible alterations in flood risk at the regional scale. Focusing on the Hanjiang river basin (HRB), this study develops a framework for establishing a scientific assessment of spatio-temporal dynamics of future flood risks under multiple future scenarios. In this framework, a GCMs statistical downscaling method based on machine learning is used to project future precipitation, the PLUS model is used to project future land use, the digitwining watershed model (DWM) is used to project future runoff, and the entropy weight method is used to calculate risk. Six extreme precipitation indices are calculated to project the spatio-temporal patterns of future precipitation extremes in the HRB. The results of this study show that the intensity (Rx1day, Rx5day, PRCPTOT, SDII), frequency (R20m), and duration (CWD) of future precipitation extremes will be consistently increasing over the HRB during the 21st century. The high values of extreme precipitation indices in the HRB are primarily located in the southeast and southwest. The future annual average runoff in the upper HRB during the near-term (2023–2042) and mid-term (2043–2062) is projected to decrease in comparison to the baseline period (1995–2014), with the exception of that during the mid-term under the SSP5-8.5 scenario. The high flood risk center in the future will be distributed in the southwestern region of the upper HRB. The proportions of areas with high and medium–high flood risk in the upper HRB will increase significantly. Under the SSP5-8.5 scenario, the area percentage with high flood risk during the future mid-term will reach 24.02%. The findings of this study will facilitate local governments in formulating effective strategic plans for future flood control management.

Keywords: extreme precipitation; runoff projection; flood risk assessment; CMIP6; climate change; Hanjiang River Basin

Citation: Wang, D.; Shao, W.; Liu, J.; Su, H.; Zhang, G.; Fu, X. Exploring Spatio-Temporal Dynamics of Future Extreme Precipitation, Runoff, and Flood Risk in the Hanjiang River Basin, China. *Remote Sens.* **2024**, *16*, 3980. https://doi.org/10.3390/rs16213980

Academic Editor: Yuriy Kuleshov

Received: 13 September 2024
Revised: 16 October 2024
Accepted: 23 October 2024
Published: 26 October 2024

1. Introduction

The regional hydrological cycles have been altered by global climate change through the influence of meteorological and hydrological factors, leading to significant changes in runoff processes, which have triggered a series of hydroclimatic extremes. Regional hydroclimatic extremes (extreme precipitation and floods), which have constrained coordinated and sustainable socio-economic development, constitute one of the most prevalent and destructive climate hazards under global climate change [1–4]. Extreme precipitation

and flooding disasters have caused 129,180 deaths and USD 614.53 billion in economic losses globally between 2000 and 2020, as reported in the Emergency Events Database (EMDAT) [5]. In addition, the World Meteorological Organization (WMO) in 2021 reported that the number of disasters, such as extreme climate and floods, had increased fivefold over the past 50 years, with total losses amounting to USD 3.64 trillion [6]. Therefore, exploring regional extreme precipitation, runoff and flood disaster risk in future is very essential to supply useful information to reduce the impacts of climate change and attain sustainable development goals [7–9].

The sixth assessment report of the Intergovernmental Panel on Climate Change (IPCC) states that the frequency and intensity of extreme precipitation events on global mainland have significantly increased since the 1980s, and there is a severe tend that will be seen in the future [10]. In recent years, numerous studies on extreme precipitation events at the global and regional scales have indicated that the rainy days and extreme precipitation events all over the world will significantly increase in the future compared with historical periods [4,11–14]. The increasing extreme precipitation events in the future will cause serious flood events, which will lead to severe socio-economic losses [8]. Therefore, investigating future extreme precipitation events is very essential to supplying useful information for mitigating flood disaster risk under climate change. There are two main types of methods for defining and quantifying extreme precipitation events, one using extreme value theory and the other based on extreme precipitation indices (EPIs) [15,16]. The EPIs are a set of 27 extreme climate change indices defined by the Expert Team on Climate Change Detection and Indices (ETCCDI) (https://etccdi.pacificclimate.org/, accessed on 10 April 2024) of the WMO regarding intensity, frequency and duration [17]. This method has been widely used for monitoring and predicting precipitation extreme feature, as it is conducive to the horizontal comparison of different climate models and regions [8,18]. Because of the complexity and variability of climate change, as well as its strong uncertainty, it is impossible to accurately predict future precipitation in the regional area. The current prediction of future precipitation is generally based on a series of scientific assumptions, and then the definition and quantification methods of extreme precipitation events are used to further anticipate possible changes in the future [19]. General circulation models (GCMs) developed under the auspices of the Coupled Model Intercomparison Project (CMIP) of the World Climate Research Programme (WCRP) are the major tools for exploring future precipitation based on recognized principles of physics and chemistry [7,20]. CMIP6 GCMs are the latest version released by CMIP, and they provide new possibilities for forecasting climate variables. CMIP6 GCMs have supplemented a number of improvements compared with the previous CMIP generations, such as finer spatial resolution, improved parameterization schemes for cloud microphysical processes, and enriched climate projection scenarios (Shared Socioeconomic Pathways and Representative Concentration Pathways, SSP-RCP) [21,22]. Despite decades of development, systematic biases and uncertainties in GCMs still exist in predicting future climate patterns at the regional scale. Therefore, numerous downscaled methods have been developed and widely used to solve this problem, like the empirical quantile mapping method (EQM), delta, machine learning algorithms, etc. [23–27].

Projecting future runoff patterns in a river basin is not only dependent on future climate scenarios, but also requires land use change scenarios, as well as hydrologic modeling. There are numerous models to simulate future land use, such as PLUS, CA-Markov, FLUS, CLUE-S, etc. Among them, the PLUS model can provide a better interpretation of different types of land use change influencing factors, and is more effectively applicable to large regions [28,29]. Hydrological models are important tools for studying hydrological laws and predicting hydrological phenomena. There are numerous hydrological models developed in previous studies, such as HBV, Tank, the Digitwining Watershed Model (DWM), TOPMODEL, SWAT, VIC, and the XAJ-RR model [30–33]. Under the impacts of global climate change and human activities, the hydrological cycle process of the watershed has changed significantly, the spatial heterogeneity of climate characteristics has become

more obvious, and the underlying surface has become increasingly complex. DWM, a distributed hydrological model, utilizes spatial interpolation methods and distributed parameter extraction techniques based on remote sensing images to characterize the spatial heterogeneity of meteorological data and capture the uniformity of underlying surface characteristic parameters [34,35]. After more than 20 years of development, DWM has been widely used in hydrological modeling in different areas and has become an important tool for hydrological cycle studies under the changing environments [34–41].

Projecting future flood disaster risk is based on the results of scientific forecasts of precipitation, runoff, GDP, population, and other elements, combined with flood disaster risk assessment methods, to predict flooding dynamics in future periods. Methods of assessing the flood risk can be categorized into four types: mathematical and statistical methods, indicator system methods, uncertainty analysis methods and scenario simulation methods [42]. The indicator system method intends to construct a flood disaster risk assessment indicator system from the aspects of disaster causing factors, disaster bearing environment, and disaster bearing bodies, and then quantify the regional flood disaster risk using the weight allocation method [43,44]. Shi et al. [45] used the indicator system method to assess the flood disaster risk of Xiamen in China under a large typhoon scenario. Mitra and Das [46] comparatively assessed the flood vulnerability of Koch Bihar using three multi-objective decision-making techniques, GIS techniques and the constructed indicator system. However, previous studies on assessing flood disaster risks mainly focused on historical periods, and the estimation of future risk situations is still relatively limited. There is an urgent need to conduct research on predicting future flood disaster risks in various areas of the world.

The Hanjiang River, largest tributary of the Yangtze River in China, lies in the climatic transition area between northern and southern regions, which is strongly affected by climate change. The Hanjiang river basin (HRB) is also the water resource for the middle route of the South-to-North Water Diversion Project (SNWD), China. In recent years, flood disasters have occurred frequently in the HRB [47]. Extreme precipitation is the primary factor contributing to flood disasters in the HRB, and the effective projection of future extreme precipitation is crucial for flood prevention in the middle reaches of the Yangtze River and water resource management in the middle route of the SNWD [48]. Therefore, changes in extreme precipitation, runoff and flooding have attracted the attention of researchers [47–50]. However, scholars have mostly focused on extreme precipitation, runoff, and floods in the HRB during the historical period, and limited studies have focused on projecting one aspect of future extreme precipitation, runoff, and flood disasters, without considering them comprehensively.

In this study, we primarily aim to establish a framework for the scientific assessment of flood disaster risk in the HRB under future scenarios. We use a statistical downscaling method developed in our previous study that combines EQM and machine learning algorithms for bias correction of the GCM precipitation outputs, and apply the EPIs to project the spatio-temporal aspects of precipitation extreme events over the HRB under future scenarios. We use the PLUS model to project the land use maps over the HRB. Then, we utilize DWM to project the future runoff in the study region. Finally, we apply the indicator system method to project the future flood disaster risk in the HRB, by integrating precipitation, land use, runoff, GDP, and population datasets under future scenarios. The objective of this study is to explore spatio-temporal dynamics of future extreme precipitation, runoff, and flood risk in the HRB under SSP-RCP scenarios.

2. Materials and Methods

2.1. Study Area

The HRB, located between 106°12′E~114°14′E and 30°8′N~34°11′N, has a drainage area of about 1.59×10^5 km^2 (Figure 1). The length of the Hanjiang River is 1577 km, and the upper reaches of the Hanjiang River = bounded by the Danjiangkou Reservoir are 925 km long, with a drainage area of 9.52×10^4 km^2 (Figure 1) [51]. The upper reaches of the HRB

are predominantly characterized by mountainous and semi-mountainous regions, whereas the middle and lower reaches consist of plain areas [52]. The elevation in these regions ranges from 0 to 3577 m (Figure 1). The HRB is in the subtropical monsoon climate zone, with obvious continental monsoon climate characteristics. The average annual temperature is between 15 and 17 °C, the average annual evaporation is 800~1300 mm, and the average annual precipitation is 700~1800 mm [53]. The precipitation occurring from May to October constitutes 70% to 80% of the total annual rainfall. Hence, approximately 75% of the annual runoff is generated by the precipitation during this period [49,52,54]. Precipitation in the HRB is mostly characterized by high intensity, short duration and a concentrated area. In addition, the slope of the upper HRB is large. The result is that the HRB is highly susceptible to floods with fast convergence rates, concentrated flood volumes and large flood peaks, causing severe flood disasters.

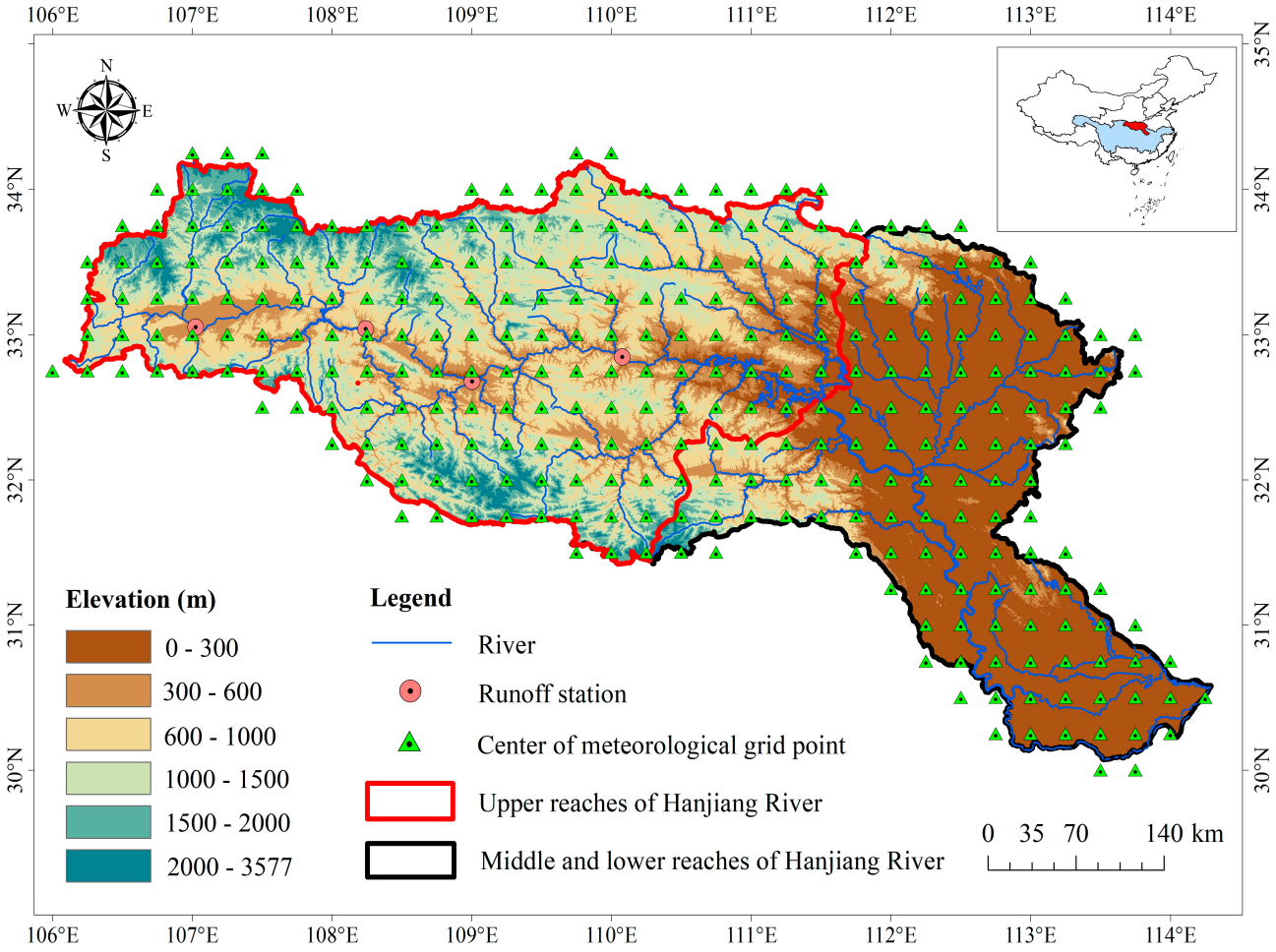

Figure 1. Location and meteorological–hydrological information of study area.

2.2. Data Acquisition

2.2.1. Hydrological Modeling Data

The data required for hydrological modeling in this study can be divided into spatial attribute data and hydrological data, as listed in Table 1. The DEM with a spatial resolution of 30 m × 30 m was obtained from the ASTER GDEM V3 elevation data shared by NASA on the Earthdata network. The land use data of the HRB for 2010 and 2020 were derived from GlobeLand30, which is extensively utilized in hydrological simulation and land use prediction [55,56]. The 2020 land use data were used for the construction of DWM in the HRB, and the two periods of 2010 and 2020 were used for the following land use simulation. The Harmonized World Soil Database 1.1 (HWSD), developed by the

Food and Agriculture Organization of the United Nations (FAO), was used to create soil parameters. Leaf area index (LAI) is a crucial parameter affecting the canopy interception and evapotranspiration processes in a watershed, and is one of the essential data types for DWM runoff calculation. For reflecting the spatial heterogeneity of LAI parameters and improving the accuracy of DWM hydrological simulation, GLASS-LAI datasets with a spatial resolution of 0.05° × 0.05° and a duration of 1995–2018 was used in this study [57]. The dataset has a high quality compared with others [58]. Since the time resolution of the GLASS-LAI dataset is 8 days, Python scripts were used to synthesize it to the monthly scale, and the difference between common year and leap year should be paid attention in the processing process. The observational precipitation data from the CN05.1 dataset for the period of 1970–2018 were utilized to conduct hydrological simulations and assess the precipitation outputs of GCMs. The CN05.1 dataset, obtained from [59], is a gridded daily observed dataset developed using the ANUSPLIN method in conjunction with the angular distance weighting technique. This dataset provides a spatial resolution of 0.25° × 0.25°, and it is based on observational data collected from 2416 national meteorological stations. Numerous studies have shown that the CN05.1 dataset features data relatively close to those obtained from meteorological stations, and have demonstrated its reliability [60,61]. A monthly potential evapotranspiration dataset (1990–2021) with a resolution 1 km × 1 km from the National Tibetan Plateau Data Center, China, was used in this study. The observed daily streamflow data of Hanzhon, Ankang, Shiquan and Baihe hydrological stations during the period of 2015–2018 were collected from the Hydrological Statistical Yearbook of the People's Republic of China for DWM parameters' calibration and model validation.

Table 1. List of hydrological modeling data.

Type		Resolution	Time	Resource
Spatial attribute data	DEM	30 m × 30 m	--	www.earthdata.nasa.gov, accessed on 5 March 2024
	Land use	30 m × 30 m	2010, 2020	https://www.webmap.cn, accessed on 5 September 2024
	Soil	1 km × 1 km	--	www.fao.org/soils-portal/so, accessed on 5 March 2024
	LAI	0.05° × 0.05°	1995–2018	www.glass.umd.edu/LAI, accessed on 5 March 2024
Hydrological data	Observed daily precipitation	0.25° × 0.25°	1970–2018	CN05.1 dataset
	Monthly potential evapotranspiration	1 km × 1 km	1995–2018	https://data.tpdc.ac.cn, accessed on 5 March 2024
	Observed daily streamflow	--	2015–2018	Hydrological Statistical Yearbook of the People's Republic of China

2.2.2. GCMs Outputs

Due to the data availability at the beginning of our previous study [52,62], daily precipitation outputs of six GCMs from CMIP6 during historical (1970–2014) and future (2015–2100) periods under three SSP-RCP scenarios, namely, SSP1-2.6, SSP2-4.5 and SSP5-8.5, were selected for projecting future precipitation patterns in this study. The precipitation outputs of CMIP6 GCMs can be obtained from https://esgf-node.llnl.gov/search/cmip6/, accessed on 5 July 2023. The basic information about the six CMIP6 GCMs is listed in Table S1, and the details can be found at https://esgf-node.llnl.gov/projects/input4mips/, accessed on 5 July 2023. The horizontal resolution of the GCMs ranges from 1.125° to 3.75° (Table S1). To ensure consistency, the precipitation output data from all GCMs were resampled to a uniform grid of 0.25° × 0.25° using bilinear interpolation in accordance with many other CMIP studies [63,64], aligning them with the observed CN05.1

resolution. It is widely recognized that the bilinear interpolation method represents the most efficient technique for resampling a grid dataset [65,66]. However, in the absence of a standardized spatial resolution, assessing the precipitation simulation capabilities of GCMs and projecting future precipitation using multi-model ensembles would be unfeasible.

2.2.3. Driving Factors of Land Use

Land use change is a complex, non-linear process that is influenced by a variety of driving factors, which can be categorized into environmental factors and socio-economic factors. Based on the actual situation in the study area, six natural environmental factors and nine socio-economic factors were selected, with reference to relevant literature [28,67] and the principles of comprehensiveness, accessibility and quantifiability. Detailed information and the data sources of driving factors are listed in Table 2. Each driving factor is processed uniformly as a 30 m × 30 m raster file in ArcGIS 10.8 under the same coordinate system, using historical land use data as the baseline. The distances to railways, railway stations, roads, and river were computed using the Euclidean distance tool in ArcGIS.

Table 2. List of the selected driving factors.

Type	Data	Resolution/Unit	Resource
Natural environmental factors	DEM	30 m × 30 m	www.earthdata.nasa.gov, accessed on 5 March 2024
	Slope	30 m × 30 m	
	Average annual precipitation	1 km × 1 km/mm	www.resdc.cn, accessed on 10 May 2024
	Average annual temperature	1 km × 1 km/°C	
	Soil	1 km × 1 km	www.fao.org/soils-portal/so, accessed on 5 March 2024
Socio-economic factors	River	m	Extracted from Globle 30 land use data
	Railway	m	OpenStreetMap www.openstreetmap.org, accessed on 10 May 2024
	Railway station	m	
	Primary road	m	
	Secondary road	m	
	Tertiary road	m	
	Trunk road	m	
	GDP	1 km × 1 km	www.resdc.cn, accessed on 10 May 2024
	POP	1 km × 1 km	
	Night lights	1 km × 1 km	

2.3. Methods

This section presents a comprehensive framework of quantifying future flood disaster risks under SSP-RCP scenarios that combines a GCMs statistical downscaling method based on EQM and multiple machine learning algorithms for projecting future precipitation, a PLUS model for simulating the land use distribution maps, a DWM for simulating hydrological processes, and the method for assessing the flood disaster risks. EPIs were used to define future extreme precipitation events based on the projection results of the future precipitation. Using the projections of future precipitation and land use, the future runoff process is obtained through DWM. Based on the future extreme precipitation, land use, and runoff, the future flood disaster risk is explored using the index system method for assessing flood disaster risk. The comprehensive framework of the methodology developed in this study is illustrated in Figure 2. It is important to note that the anticipated future changes in runoff and flood risk are evaluated against historical data covering a period of 20 years, specifically from 1995 to 2014, in this study. The chosen baseline period of 1995–2014 is in alignment with the IPCC AR6 report. Under the SSP-RCP scenarios, the future time periods of 2023–2042 and 2043–2062 in this study were defined as "near-

term" and "mid-term", respectively. Considering the national policies control on land use expansion, the observed land use data in 2020 and the predicted land use data in 2040 are taken as the future land use scenarios during the near-term and mid-term, respectively.

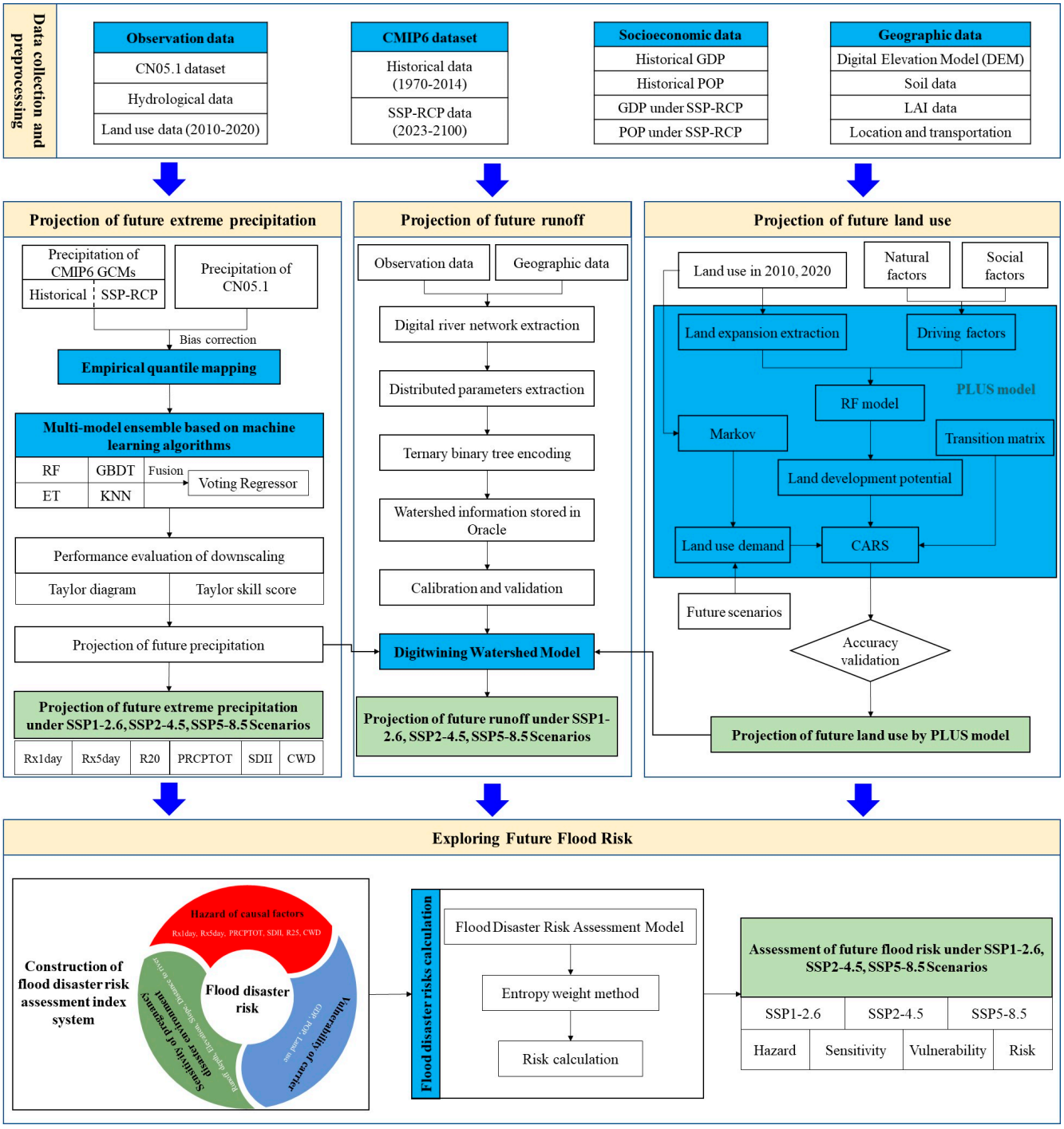

Figure 2. Overall framework of the methodology.

2.3.1. Statistical Downscaling Method for GCMs Precipitation

The statistical downscaling method used in this study integrates a bilinear spatial interpolation method, an EQM bias correction method, and a multi-model ensemble method based on fusion of multiple machine learning algorithms. This statistical downscaling method was proposed in our previous study, and has been proven to be applicable using the Taylor diagram and Taylor skill score [52]. The methodological framework can be

divided into three main steps: (1) precipitation outputs from each GCM are bias-corrected based on EQM method to reduce the systematic bias of the GCMs; (2) the Random Forest, K-Nearest Neighbors, Extra Tree and Gradient Boosting Decision Tree are fused to perform multi-model ensembles of GCMs bias-corrected results to further reduce the simulation bias and the uncertainty of individual GCM simulations; (3) finally, the downscaled results are evaluated and future precipitation changes in the watershed are projected. Details about above method can be found in [52]. Additionally, the future precipitation under SSP1-2.6, SSP2-4.5 and SSP5-8.5 in the HRB has been projected based on the GCMs outputs using the above statistical downscaling method in our previous study [52]. In this study, future extreme precipitation changes in the HRB will be analyzed with emphasis on the future precipitation projection data.

2.3.2. Selection of the Extreme Precipitation Indices

Based on the environmental conditions of the HRB, six standard EPIs with high impact on flood risk were selected in this study, namely, Rx1day, Rx5day, PRCPTOT, SDII, R20, and CWD, to quantify the precipitation extremes in HRB over 1995–2100. The detailed information is listed in Table 3 [8,68]. The six selected EPIs can be categorized into three types, i.e., intensity index, duration index, and frequency index. The EPIs were calculated based on the R Programming Language. The Mann–Kendall method and the Theil–Sen Median method were used to calculate the inter-annual change trends and to determine the significance of each index.

Table 3. List of the selected EPIs.

Type	Index	Definition	Unit
Intensity index	RX1day	Maximum daily precipitation	mm
	RX5day	Maximum consecutive 5-day precipitation	mm
	PRCPTOT	Total precipitation during wet days	mm
	SDII	Average precipitation during wet days	mm/day
Frequency index	R20mm	Number of days with precipitation equal to or exceeding 20 mm	day
Duration index	CWD	Maximum number of consecutive days with precipitation measuring at least 1 mm	day

2.3.3. Future Land Use Projection by PLUS Model

The PLUS model was selected to project the future land use maps in the HRB. The main steps of PLUS modeling are as follows (Figure 2): (1) Each land use change area is extracted based on the two periods of observed land use data. Then, the Random Forest model driven by the natural environment and socio-economic driving factors is used to excavate the impacts of various factors on land use change, and to generate the potential development probability for each type of land use. (2) The Markov Chain model is utilized to forecast land use development demand. Combining with the potential development probability, a CA model that utilizes multiple types of stochastic patch seeds is employed to forecast future spatial distributions of land use. The details can be found in [9,28]. Compared with other models, it can be better applied to large-scale regions and the simulation results are more accurate [28,29].

In this study, we initially validated the accuracy of the PLUS model and subsequently predicted the land use map in 2040. The entire process can be categorized into the following steps: (1) The prediction of land use in 2020 was conducted using the observational land use maps in 2010 and 2020, and then the model's accuracy was assessed through a comparison with the observed land use in 2020. (2) The land use development demand over the HRB in 2040 was calculated using the Markov Chain. In this step, the conversion probabilities

of forest land, grass land and water to urban land were reduced by 20% based on a series of programs and policies for ecological conservation. (3) The land use map over the HRB in 2040 was projected by using the PLUS model based on the 2020 land use data, the development probability and the development demand.

The Kappa indices were selected to assess the accuracy of land use simulation results produced by the PLUS model. The value of Kappa indices spans from 0 to 1. A value closer to 1 indicates a higher level of simulation accuracy. In general, when the Kappa indices are greater than or equal to 0.75, it indicates a strong correlation between the simulated map and the observed map [69]. The comprehensive details of the Kappa indices can be found in [70].

2.3.4. Hydrological Simulation by DWM

The DWM was developed by Tsinghua University in China, and is a distributed hydrological model mainly composed of hillside hydrological simulation and river network routing [71–73]. This model uses high-resolution digital drainage networks extracted from DEM data and encoded using the binary tree coding method to simulate hydrological processes. Furthermore, parameter extraction technology utilizing remote sensing imagery, along with dynamic parallelism techniques based on sub-basin decomposition, have been developed to efficiently extract distributed parameters of the sub-basins and expedite the hydrological simulation process.

The DWM employs the hillslope-channel as a fundamental hydrological response unit, regarding the distinct hydrological response mechanisms in both hillslopes and channels [39]. The runoff generation process of the DWM is carried out on an individual hillslope, including sub-processes such as vegetation retention, evapotranspiration and infiltration. The flow concentration of the DWM is the evolution of water flow to the outlet of the basin step by step according to the sequence of the river network, and the simulation time step can be as fine as 6 min. The detailed information about DWM will not be repeated in this study. However, it is worth noting that the parameters in DWM are mainly divided into two categories. One is the fixed parameters used to describe hydrogeological information such as soil type, vegetation cover, and land use type. These parameters can be obtained through the observed data or field experiments. The other is the sensitivity parameters that need to be calibrated and validated using observed precipitation and runoff data, such as saturated hydraulic conductivity, water content, Manning's coefficient, etc.

The DWM was used in this study to simulate the hydrological processes in the upper HRB. To ensure the model accurately reflects hydrological processes, it was calibrated and validated during the historical period before being employed to simulate future hydrological changes. Observed daily streamflow data during the period of 2015–2018 from four hydrological stations (Hanzhong, Ankang, Shiquan, and Baihe) in the upper HRB were used for DWM parameters calibration. Hanzhong station, located at the source of Hanjiang River, is less affected by human activities such as reservoir storage. Therefore, this study utilizes the observed streamflow data from Hanzhong station during 2015–2016 to calibrate the parameters, focusing on the simulation effect of Hanzhong station. The daily streamflow data during 2017–2018 from Hanzhong, Shiquan, Ankang and Baihe stations were utilized to validate the reliability of DWM in the upper HRB. To evaluate the performance of hydrological simulation using DWM, the coefficient of determination (R^2), the Nash–Sutcliffe coefficient of efficiency (NSE), and PBIAS were used in this study. The equations are as follows:

$$R^2 = \left[\frac{\sum_{i=1}^{n} \left(O_i - \overline{O}\right)\left(S_i - \overline{S}\right)}{\left(\sum_{i=1}^{n} \left(O_i - \overline{O}\right)^2 \sum_{i=1}^{n} \left(S_i - \overline{S}\right)^2 \right)^{0.5}} \right]^2 \quad (1)$$

$$NSE = 1 - \left[\frac{\sum_{i=1}^{n} (O_i - S_i)^2}{\sum_{i=1}^{n} (O_i - \overline{O})^2} \right] \quad (2)$$

$$PBIAS = \left[\frac{\sum_{i=1}^{n} (O_i - S_i) \times 100}{\sum_{i=1}^{n} (O_i)} \right] \quad (3)$$

where O_i and S_i refer to the observed and simulated daily runoff, respectively, and $\overline{O}$ and $\overline{S}$ refer to the mean values of the observed and simulated daily runoff, respectively. The evaluation standards are as follows: good ($R^2 > 0.8$, NSE > 0.7), satisfactory ($0.5 < R^2 \leq 0.8$, $0.4 < NSE \leq 0.7$) and unsatisfactory ($R^2 \leq 0.5$, NSE ≤ 0.4) [74]. In addition, when PBIAS $\leq 25\%$, it indicates that the simulation results are acceptable.

2.3.5. Flood Disaster Risk Projection and Analysis Method

The flood disaster risk projection and its analysis method over the HRB used in this study include the following: (1) Establishment of a flood disaster risk evaluation indicators system that incorporates hazard, sensitivity, and vulnerability factors. (2) Determination of each indicator weight utilizing the entropy weight method based on multi-source projection dataset. (3) Visualization of the spatial dynamics of flood risk in the upper HRB during the near-term (2023–2042) and mid-term (2043–2062) under SSP1-2.6, SSP2-4.5, and SSP5-8.5 scenarios. The flood disaster risk in this study is a comprehensive function of the hazard, sensitivity and vulnerability [75]. The flood disaster risk level was defined as high level, medium–high level, medium level, and low level using the natural breakpoint method in the ArcGIS. The equations are as follows:

$$H_{(x)} = \sum_{j=1}^{i} w_i H_{ji(x)} \quad (4)$$

$$S_{(x)} = \sum_{j=1}^{i} w_i S_{ji(x)} \quad (5)$$

$$V_{(x)} = \sum_{j=1}^{i} w_i V_{ji(x)} \quad (6)$$

$$R_{(x)} = H_{(x)} \times S_{(x)} \times V_{(x)} \quad (7)$$

where $R_{(x)}$, $H_{(x)}$, $S_{(x)}$, and $V_{(x)}$ are the comprehensive flood disaster risk, hazard risk, sensitivity risk and vulnerability risk, respectively. $H_{ji(x)}$, $S_{ji(x)}$ and $V_{ji(x)}$ are the standardized values of each indicator. w_i is the weight assigned to each indicator using the entropy weight method.

Starting from the formation mechanism of flood disaster, 13 flood risk assessment indicators were selected in this study considering the natural–social factors and the availability of indicator data based on the reference of existing flood disaster risk assessment studies [43,76]. The hazard factors included the Rx1day, Rx5day, PRCPTOT, SDII, R20 and CWD, which were calculated based on the precipitation data during the period of 1995–2062 (Figures S1–S4). The sensitivity factors included the runoff depth, elevation (DEM) (Figure 1), slope (Figure S5c), and distance to river (DR) (Figure S5d). The runoff depth was calculated by the ratio of the runoff results simulated by DWM and the area of hillslope (left slope, right slope and source slope). The vulnerability factors included the GDP, POP, and land use. The GDP and POP data were obtained from a gridded dataset developed by Nanjing University of Information Engineering, China under different SSPs scenarios (https://cstr.cn/31253.11.sciencedb.01683, accessed on 5 July 2023). The dataset was produced after a long period of research and exploration supported by several interna-

tional and national projects, and includes global POP and GDP grid point projection for 2020–2100 under SSP1 to SSP5 scenarios at a resolution of 0.5° × 0.5° [77] (Figure S6). Each factor was converted to a raster file and the resolution was resampled to 1 km × 1 km with a total grid count of 95,200, depending on the size of the study area.

The entropy weight method was applied to assign the weights of each indicator in this study. Before determining the weight values, it is necessary to normalize the raw data. In this study, the min–max standardization method was used to normalize the source data of each indicator. The standardized value is located between 0 and 1, with a value closer to 1 indicating higher risk. Among the selected indicators, Rx1day, R95p, PRCPTOT, SDII, R25, CWD, runoff depth, land use, GDP, and POP are positive indicators, and DEM, slope, and DR are negative indicators. Due to the different degrees of disaster losses for different land use types, cultivated land and urban land were set as high risk, wet land and water were set as medium–high risk, grass land was set as medium level risk, and wood land and bare land were set as low risk. The entropy weight method included the following: (1) A judgment matrix with $m \times n$ evaluation indicators is constructed, shown in Equation (8). (2) The weight p_{ij} of the ith indicator in the jth indicator is determined by Equation (9). (3) The entropy value e_j of the jth indicator is determined by Equation (10). (4) The information entropy redundancy d_j of the jth indicator is determined by Equation (11). (5) Finally, the entropy weights w_j of each indicator can be obtained by Equation (12).

$$X = \left(Z_{ij}\right)_{m \times n} \tag{8}$$

$$p_{ij} = \frac{Z_{ij}}{\sum_{i=1}^{n} Z_{ij}} \tag{9}$$

$$e_j = -\frac{1}{\ln m} \sum_{i=1}^{m} p_{ij} \ln p_{ij} \tag{10}$$

$$d_j = 1 - e_j \tag{11}$$

$$w_j = \frac{d_j}{\sum_{j=1}^{n} d_j} \tag{12}$$

3. Results

3.1. Future Projection of Extreme Precipitation

The temporal evolutions of Rx1day, Rx5day, PRCPTOT, SDII, R20 and CWD in HRB during the period of 2023–2100 under the SSP1-2.6, SSP2-4.5 and SSP5-8.5 scenarios are presented in Figure 3. The tables in Figure 3 show the Mann–Kendall test statistic Z and Sen's slope for each index, respectively. It is evident that the EPIs in HRB will show fluctuating changes in the future compared with the historical period, indicating that the extreme precipitation events will become unstable. The Rx1day, Rx5day, PRCPTOT, SDII, and R20 under the SSP5-8.5 scenario are more destabilizing than the two scenarios. The six EPIs in HRB over 2023–2100 under the three scenarios show a rising trend. Except for no significant increase in Rx5day under SSP1-2.6 scenario, and CWD under SSP1-2.6 and SSP2-4.5 scenarios, the other extreme precipitation indicators in HRB over 2023–2100 under the three scenarios show a significant increase trend. It also can be found from the Figure 3 that the increase in the magnitude of the six EPIs in HRB from 2023 to 2100 is most pronounced under the SSP5-8.5 scenario, followed by the SSP2-4.5 scenario, while the smallest increase is seen under the SSP1-2.6 scenario. Except for the CWD, the increase trends of all other EPIs for SSP5-8.5 are more than those for SSP2-4.5 and SSP1-2.6, especially during the period of 2070–2100. The increases in Rx1day, Rx5day, PRCPTOT, SDII, R20 and CWD under the SSP5-8.5 scenario are 4.6 mm/10 a, 7.2 mm/10 a, 61.6 mm/10 a, 0.3 mm/day/10 a, 1 day/10 a and 0.2 day/10 a, respectively.

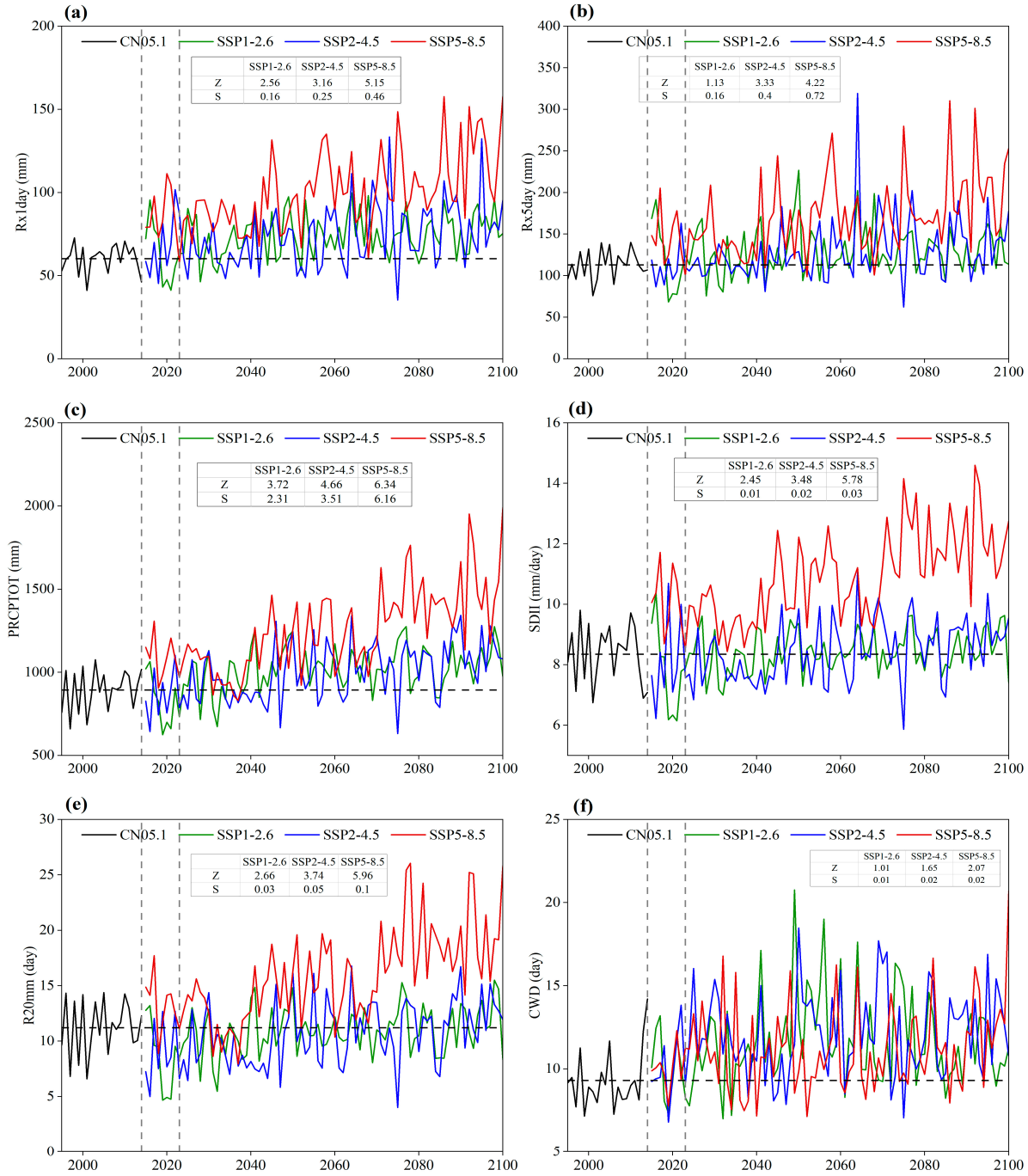

Figure 3. Temporal evolution of Rx1day (**a**), Rx5day (**b**), PRCPTOT (**c**), SDII (**d**), R20mm (**e**), and CWD (**f**) during 1995–2014 and 2023–2100 under the three SSP-RCP scenarios. The tables display the Mann–Kendall test statistic Z and Sen's slope.

The spatial distributions of the six EPIs in HRB during future (2023–2100) and historical (1995–2014) periods under the SSP1-2.6, SSP2-4.5 and SSP5-8.5 scenarios are illustrated in Figure 4. It can be found that spatial patterns of the six EPIs in future under the three SSP-RCP scenarios are consistent with historical distributions. The high values of Rx1day, Rx5day, SDII and R20mm during periods of 1995–2014 and 2023–2100 are concentrated in the southeast and west of the basin, which are areas with high urbanization. The values of PRCPTOT in the southeastern and southwestern regions of the basin are higher than in other areas. As to CWD, the southwest of the study region has a higher value than other areas. Figure 4 also illustrates Box–Whisker plots of the EPIs during 2023–2100 and

1995–2014. The Boxes illustrate the range encompassed by the 25th and 75th quantiles, while the Whiskers indicate the span between the minimum and maximum values. The mean values of Rx1day, Rx5day, PRCPTOT, and SDII projected for the future under the three SSP-RCP scenarios are significantly higher than in historical times. The values of these four EPIs are the highest under the SSP5-8.5 scenario, which were 101.36 mm, 170.82 mm, 1262.53 mm, and 10.95 mm/day, respectively. The mean of R20mm is the highest over 16 days in a future period of 2023–2100 under the SSP5-8.5 scenario, followed by the historical period from 1995 to 2014, and is lowest in a future period under the SSP1-2.6 and SSP2-4.5 scenarios. As to CWD, the mean value in the future is highest at 12.13 days under the SSP2-4.5 scenario.

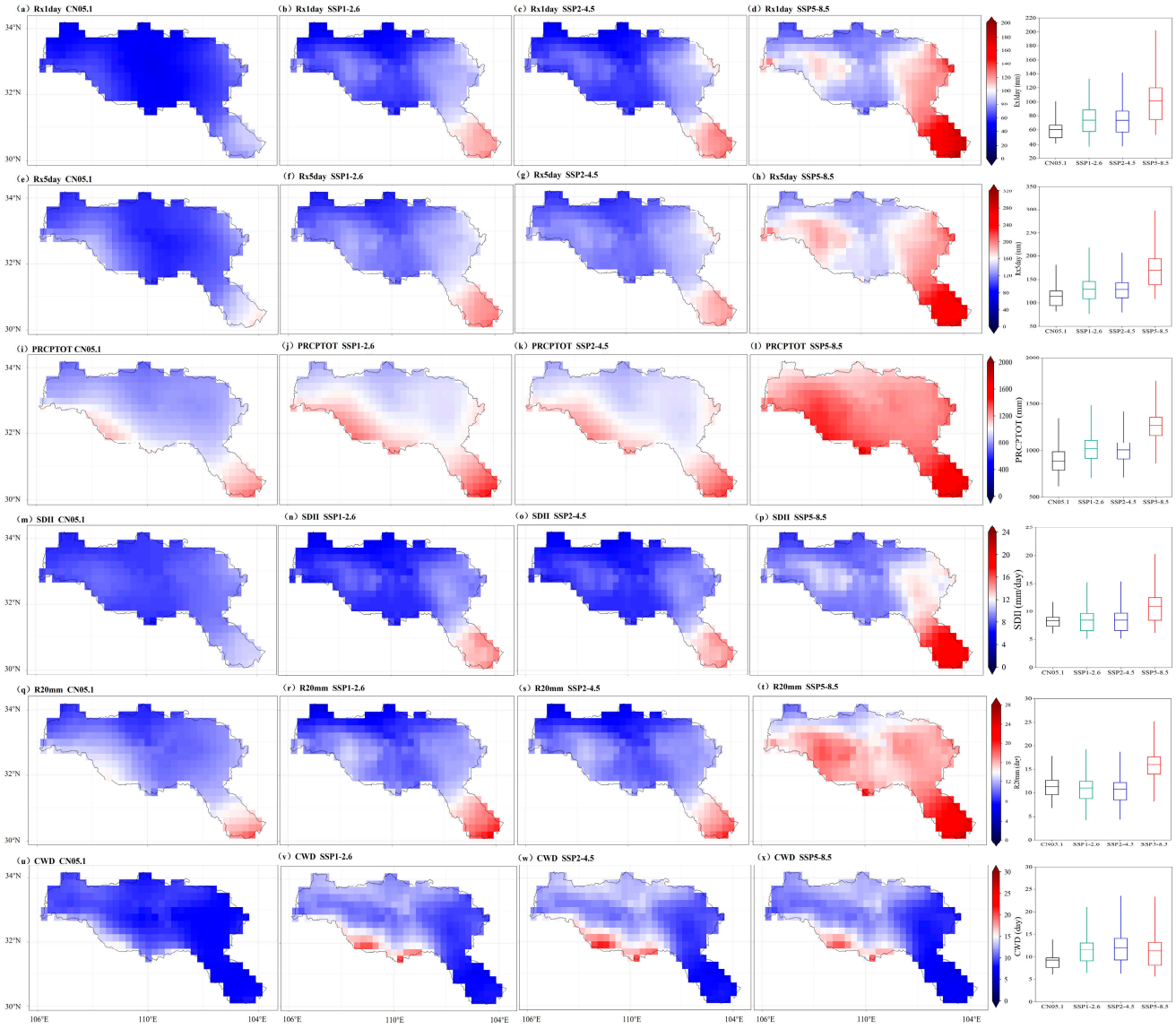

Figure 4. Spatial patterns and box plots of EPIs during 1995–2014 and 2023–2100 under the three SSP-RCP scenarios.

3.2. Future Projection of Land Use

Based on land use maps in 2010 (Figure 5a) and 2020 (Figure 5b), the land use distribution in 2040 (Figure 5d) under the combined influence of the above 15 driving factors and the series of policies for ecological conservation are simulated. By setting the parameters of the PLUS model, the land use pattern in 2020 (Figure 5c) was simulated and the observed land use data in 2020 were compared with the simulation results. The Kappa coefficient is

0.796, indicating a higher level of prediction accuracy. The simulation of a land use map in 2040 (Figure 5d) is reliable. It can be seen that the wood land, grass land and other areas being occupied by urban land are reduced in the 2040 simulated land use map, and the rapid expansion of urbanization will be controlled under the ecological conservation scenario.

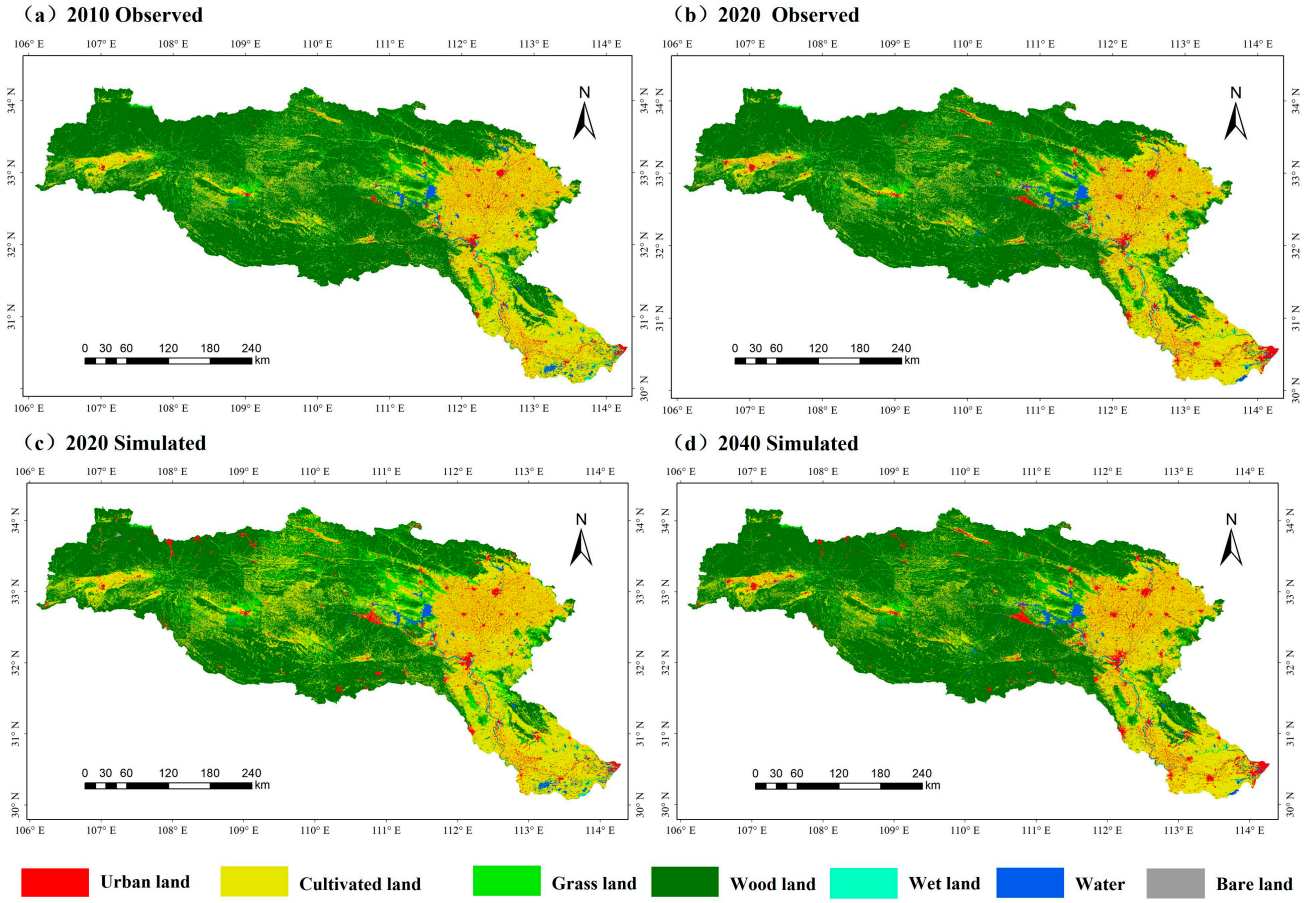

Figure 5. Observation land use map in 2010 and 2020, and simulation results in 2020 and 2040.

Figure 6a shows the contribution of each driving factor to the expansion of different land use types. It is observable that the principal driving factors influencing the expansion of cultivated land are the distance to water, DEM, and average annual precipitation. Among these, the distance to water has the most significant impact on the expansion of cultivated land, as the survival of crops is highly dependent on the water supply. The expansion of wood land is primarily influenced by DEM, distance to water, POP and slope, with DEM exerting the most significant impact on the expansion. In addition, DEM also constitutes the most influential driving factor for grass land expansion, followed by average annual precipitation and distance to water. Regarding urban land, its expansion is closely associated with night lights, and is also influenced by DEM and distance to water, followed by distances to roads at all levels and GDP. Night lights data can reflect the degree of population aggregation. It can be seen that population aggregation plays a leading role in urban expansion. Figure 6b presents the variation of land use types during the period from 2020 to 2040. Between 2020 and 2040, 0.77% of cultivated land, 0.83% of wood land, and 0.22% of grass land convert to urban land under the ecological environment protection scenario, while 1.06% of grass land converts to wood land.

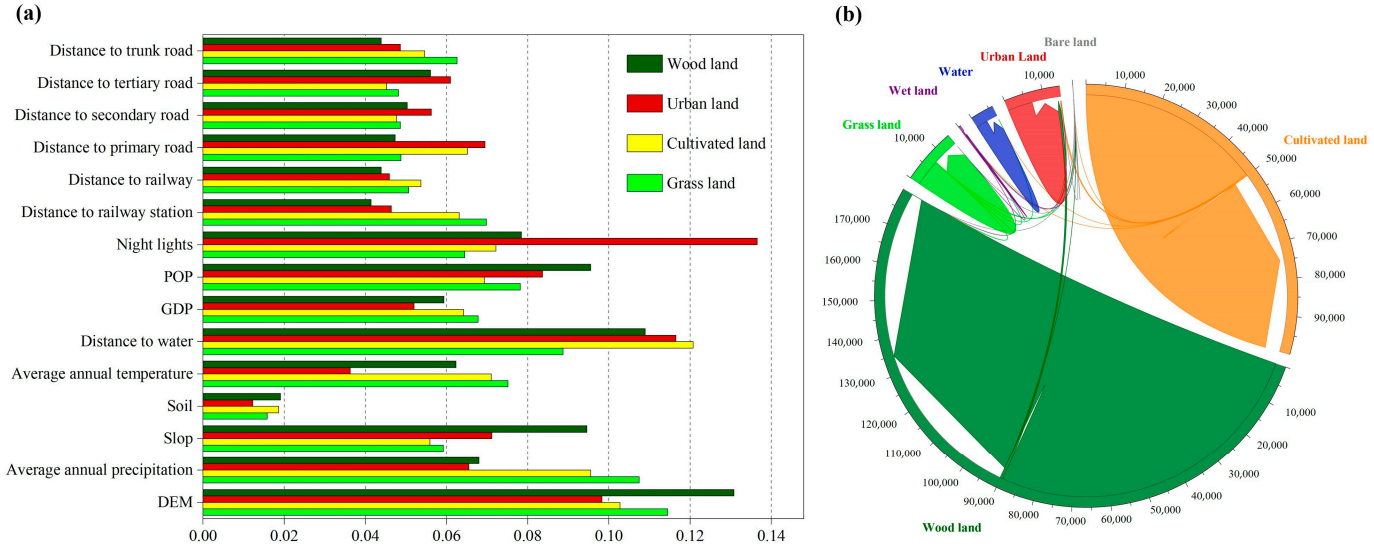

Figure 6. (**a**) Contribution of each driving factor to the expansion of wood, urban, cultivated and grass land, and (**b**) variation in land use types during period of 2020–2040.

3.3. Future Projection of Runoff

3.3.1. Calibration and Validation of DWM

Based on the observed daily streamflow data from Hanzhong, Ankang, Shiquan, and Baihe stations in the upper HRB, the DWM was calibrated and validated. The calibrated values of sensitivity parameters in DWM are shown in Table 4. The runoff simulation capacity of DWM during the calibration and validation periods was quantitatively assessed through the utilization of R^2, NSE, and PBIAS, whose calculation results are presented in Table 5. It can be seen that both R^2 and NSE of Hanzhong Station exceeded 0.7 during the calibration period, and PBIAS amounted to 22.34%, which is less than 25%. Although the PBIAS of Hanzhong Station during the calibration period was marginally larger, it remained within an acceptable range, suggesting that the calibrated uncertain parameters can better mirror the actual situation in the upper reaches of the HRB. The application of this set of parameters for runoff simulation yields a favorable effect. The R^2 and NSE of all stations during the validation period exceeded 0.6, and the absolute values of PBIAS were less than 15%. Among these, the NSE of Hanzhong Station reached as high as 0.81, and the R^2 reached as high as 0.83 during the validation period. However, the NSE values of Ankang and Baihe were marginally lower, both at 0.64. This might be influenced by the regulation and storage of large reservoirs in Shiquan and Ankang. The reservoir capacity of Ankang Reservoir can reach 2.585 billion m^3, exerting a significant influence on the runoff of the downstream basin.

Figure 7 depicts the daily simulated and measured runoff process curves at each station during the calibration and validation periods. It can be seen that the simulated and measured daily discharge process curves at the four hydrological stations are in accordance during the calibration and validation periods, indicating that DWM is capable of better capturing the daily runoff variations of the hydrological stations in the basin. The simulated trend of runoff is essentially consistent with the measured trend, and the simulation effect is favorable. Additionally, DWM possesses a remarkable capacity to capture runoff during the wet season, particularly with regard to the recurrence of peak values. It is worth noting that the capacity of DWM to capture the actual runoff is moderately weak during the dry season spanning from December to March of the subsequent year, particularly at the Ankang and Baihe stations. This is primarily attributed to the regulation and storage functions of large reservoirs such as Shiquan and Ankang in the upper reaches.

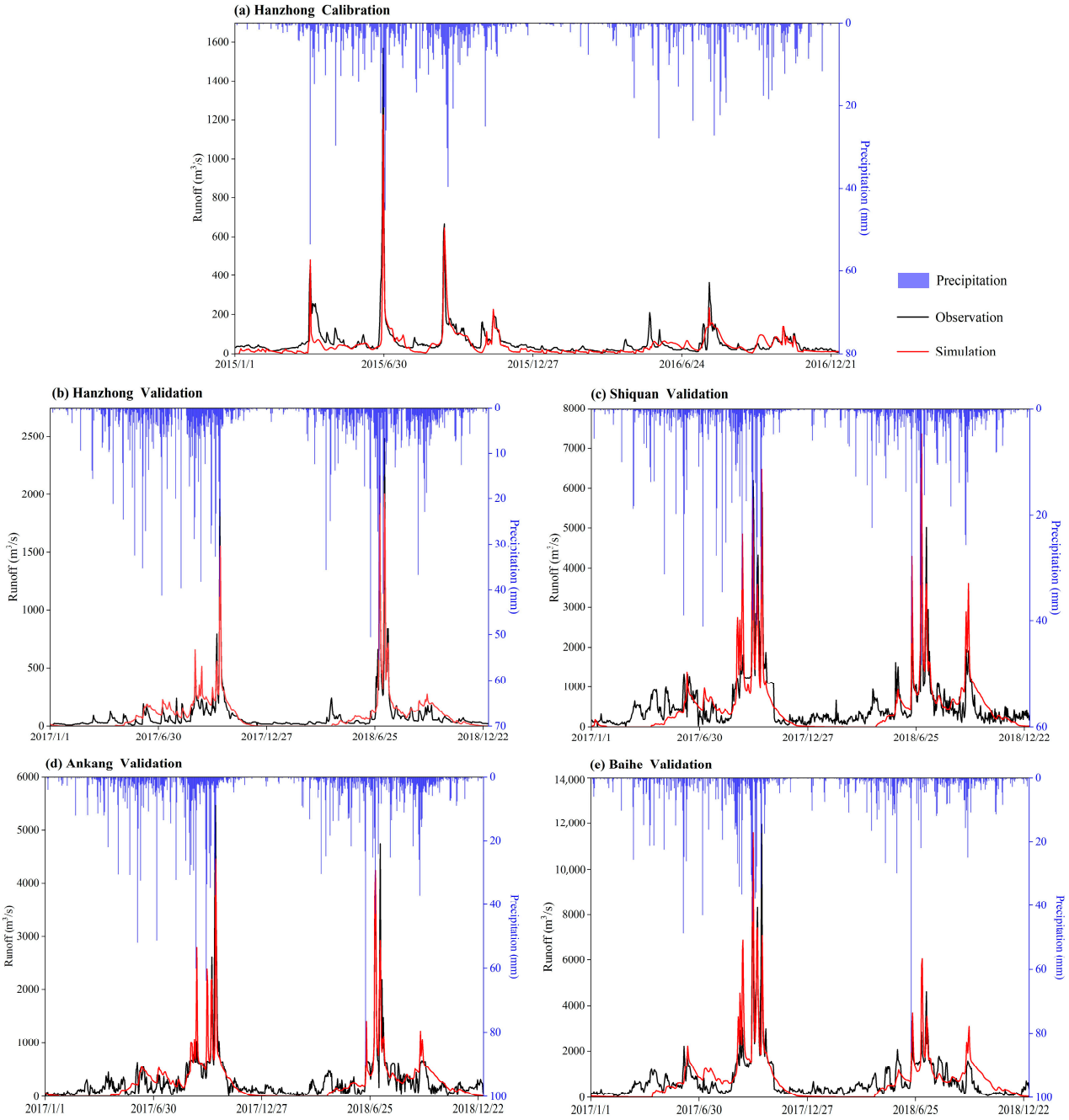

Figure 7. Simulated and measured runoff process curves at Hanzhong, Shiquan, Ankang and Baihe stations during calibration and validation periods.

Based on the validated DWM, the downscaling results of precipitation data from 2023 to 2062 under the three SSP-RCP scenarios, the observed land use data in 2020 and the simulated land use data in 2040 were employed to drive DWM. The daily runoff processes under the three SSP-RCP scenarios over the upper HRB during the future near-term (2023–2042) and mid-term (2043–2062) were simulated. The measured data of land use in 2020 were employed in the near-term, and the simulated data of land use in 2040 were utilized in the mid-term.

Table 4. List of the DWM sensitivity parameters.

ID	Name	Range	Initial Value	Calibrated Value
1	K_{zus}	10^{-4}~10^{-1}	4.5×10^{-4}	8.5×10^{-4}
2	$K_{u\text{-}ds}$	10^{-3}~10^{-1}	2×10^{-4}	1.3×10^{-4}
3	K_{hu}	10^{-8}~10^{-1}	9.8×10^{-8}	9.9×10^{-3}
4	K_{hd}	10^{-8}~10^{-1}	6×10^{-8}	6×10^{-4}
5	$\theta_{u,1}$	0.1~0.5	0.2	0.42
6	$\theta_{u,2}$	0.15~0.6	0.3	0.58
7	$\theta_{d,1}$	0.1~0.5	0.2	0.475
8	$\theta_{d,2}$	0.15~0.6	0.3	0.325
9	n	--	0.1	0.029

Table 5. Performance assessment of DWM simulation results.

Indices	Calibration (2015–2016)	Validation (2017–2018)			
	Hanzhong	Hanzhong	Shiquan	Ankang	Baihe
R^2	0.75	0.83	0.72	0.72	0.68
NSE	0.73	0.81	0.70	0.64	0.64
PBIAS/%	22.34	−14.03	5.05	9.16	1.46

3.3.2. Trend Analysis of Future Runoff Variation

Figure 8 presents the variations of precipitation and runoff in the upper HRB during the near-term (2023–2042) and mid-term (2043–2062) under the SSP1-2.6, SSP2-4.5, and SSP5-8.5 scenarios in comparison with the baseline period (1995–2014). The table in Figure 8 shows the Mann–Kendall test statistic Z and Sen's slope of runoff change from 2023 to 2062 under the three scenarios. It can be found that the annual runoff changes during 2023–2062 under the three scenarios show an insignificant increasing trend over time. The increase rates of annual runoff under SSP1-2.6, SSP2-4.5, and SSP5-8.5 scenarios are 0.43%/a, 0.36%/a, and 0.49%/a, respectively. Based on the temporal evolution processes of precipitation and runoff in the upper HRB, a strong response relationship exists between them. Under the SSP1-2.6, SSP2-4.5, and SSP5-8.5 scenarios, the ranges of annual precipitation variations in the upper reaches of the HRB from 2023 to 2062 are −22.60% to 39.67%, −32.04% to 43.68%, and −19.98% to 61.87%, respectively, and the ranges of annual runoff alterations are −57.40% to 37.02%, −62.81% to 35.33%, and −48.28% to 68.05%, respectively. In comparison to the baseline period, the annual average runoff in the upper HRB during the near-term under the three SSP-RCP scenarios decreased by −19.64%, −19.33%, and −6.63%, respectively. Moreover, the annual average runoff in the mid-term under the SSP1-2.6 and SSP2-4.5 scenarios also showed decreases, with magnitudes of −9.33% and −10.48%, respectively. However, under the SSP5-8.5 scenario (extremely high emission), the annual average runoff in the mid-term demonstrates an increase of 15.66%. Overall, the annual average runoff of the upper HRB in the near-term and mid-term will decline compared with the baseline period. However, the trend in runoff from 2023 to 2062 will show a non-significant increasing trend, and its variation will be consistent with precipitation.

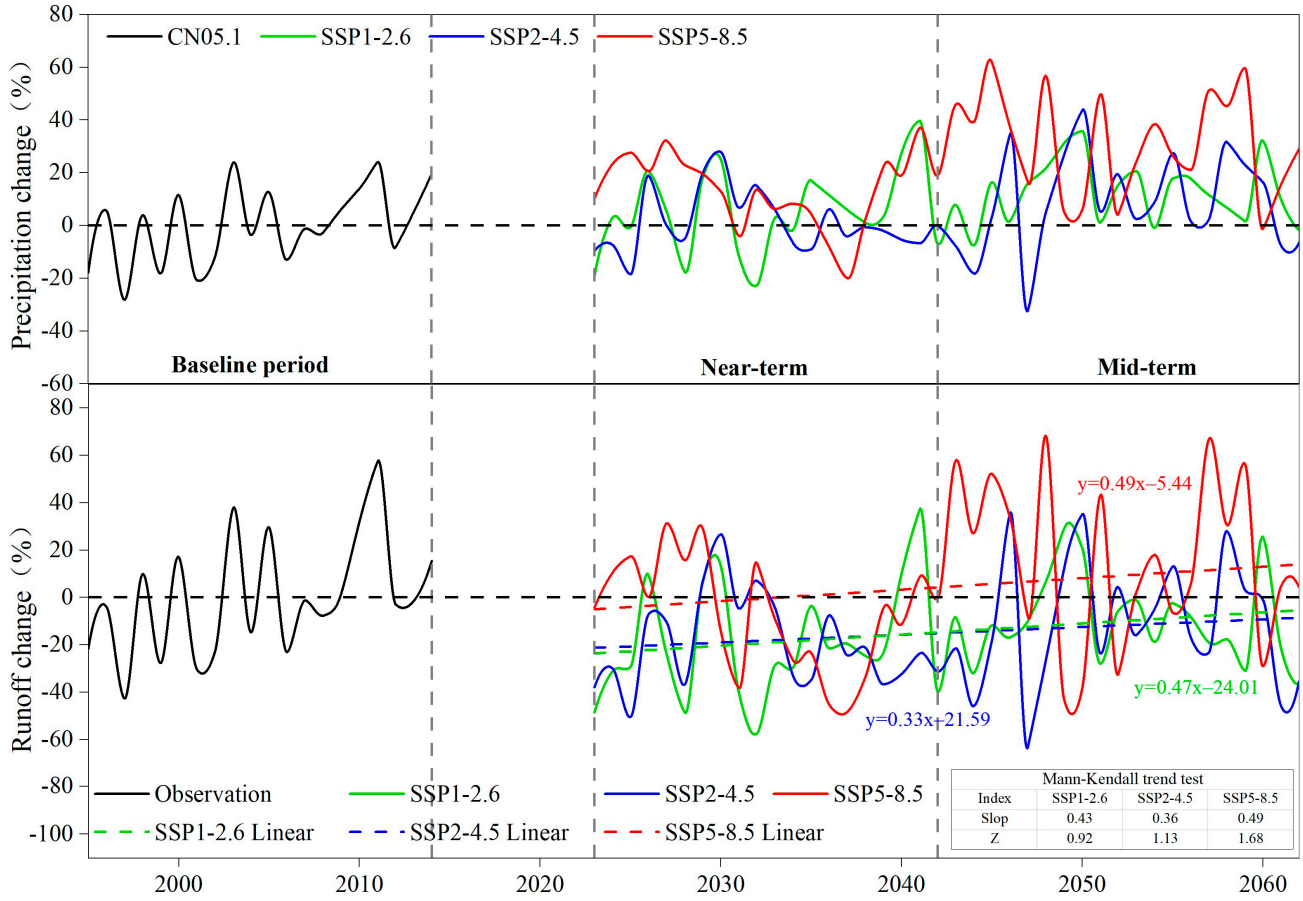

Figure 8. Temporal evolution of precipitation and runoff during period of 2023–2062 (relative to 1995–2014) in the upper HRB under the three SSP-RCP scenarios. The table displays the Mann–Kendall test statistic Z and Sen's slope of runoff change.

3.3.3. Spatial Distribution of Future Runoff Variation

Figure 9 presents the spatial patterns of the average annual runoff depth during the baseline period (1995–2014), near-term (2023–2042) and mid-term (2043–2062) under three SSP-RCP scenarios. It can be found that the spatial patterns of average annual runoff depth in the upper HRB during the near-term and mid-term under the three SSP-RCP scenarios are consistent with the baseline period. The spatial patterns of average annual runoff depth in each period show a gradient decreasing trend from southwest to northeast. In the baseline period, the annual runoff depth in the upper HRB ranges from 218.92 to 706.68 mm, and the average annual runoff depth is 377.66 mm. In the near-term, the annual runoff depth in virtually all regions of the upper HRB will diminish in contrast to the baseline period, except for a minor area under the SSP5-8.5 scenario. The variations of the annual runoff depth during the near-term under the SSP1-2.6, SSP2-4.5, and SSP5-8.5 scenarios relative to the baseline period are −29.06% to −10.60%, −35.28% to −13.33%, and −16.44% to 4.86%, respectively. The area with the largest reduction in annual runoff depth is primarily situated in the source region of the HRB. Furthermore, it can be discerned that the decline in annual runoff depth in the near-term is most pronounced under the SSP2-4.5 scenario, followed by the SSP1-2.6 scenario, and it is least significant under the SSP5-8.5 scenario. The variations in annual runoff depth during the mid-term under the SSP1-2.6, SSP2-4.5, and SSP5-8.5 scenarios relative to the baseline period are −19.86% to 9.90%, −22.49% to 5.98%, and −11.27% to 55.77%, respectively. The proportion of the area where the annual runoff depth will increase in the mid-term is highest under the SSP5-8.5 scenario, followed by the SSP1-2.6 scenario, and lowest under the SSP2-4.5 scenario. By comparing variations of the annual runoff depth during the near-term and nid-term under

the same precipitation scenario, it can be found that the area where runoff will decrease in the near-term is greater than that in the mid-term. In other words, the runoff in the upper HRB will recover during the mid-term, especially under the SSP5-8.5 scenario.

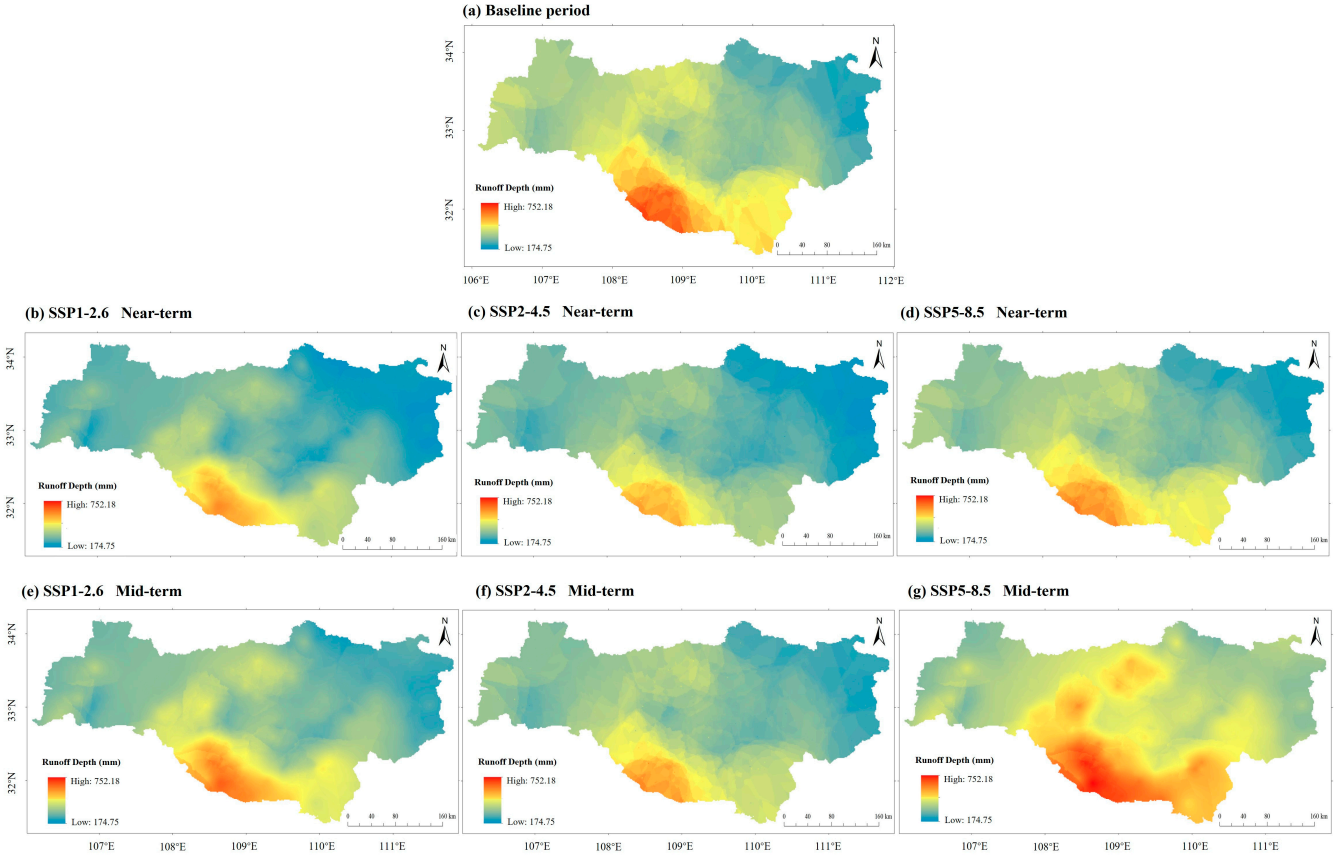

Figure 9. Geographic distributions of average annual runoff depth in the upper HRB during baseline period (1995–2014), near-term (2023–2042) and mid-term (2043–2062) under the three SSP-RCP scenarios.

3.4. Future Projection of Flood Risk

3.4.1. Hazard Indicators

Figure 10 presents the spatial maps of hazard indicators in the upper HRB during the baseline period (1995–2014), near-term (2023–2042) and mid-term (2043–2062) under the three SSP-RCP scenarios. The maps illustrate the areas that are likely to experience flood events with greater frequency. It can be seen that the spatial distributions of flood hazards across different periods and under different scenarios exhibit a consistent pattern. The high-risk areas are predominantly concentrated in the southwestern area of the basin, while the risk in the northern area is low. The flood hazard risks exhibit a tendency of gradually decreasing from the high-risk center to the surrounding regions. Figure 10 also shows the area percentage of different risk zones under different scenarios during different periods. It can be seen that the proportion of high-risk and medium–high-risk areas in the future period will be higher than that in the baseline period, indicating that the flood hazard of the upper HRB will further increase during the future near-term and mid-term. In the future near-term, the area percentage of high-risk areas will be the largest under the SSP5-8.5 scenario (21.98%), followed by the SSP1-2.6 scenario (20.20%), while it will be smallest under the SSP2-4.5 scenario (18.17%). In the future mid-term, the area percentage of high-risk areas will be the largest under the SSP5-8.5 scenario (23.46%), followed by the SSP2-4.5 scenario (22.82%), and it will be the smallest under SSP1-2.6 (19.04%). Under

the SSP2-4.5 and SSP5-8.5 scenarios, the proportion of high-risk areas will further increase during the future mid-term compared with that during the near-term.

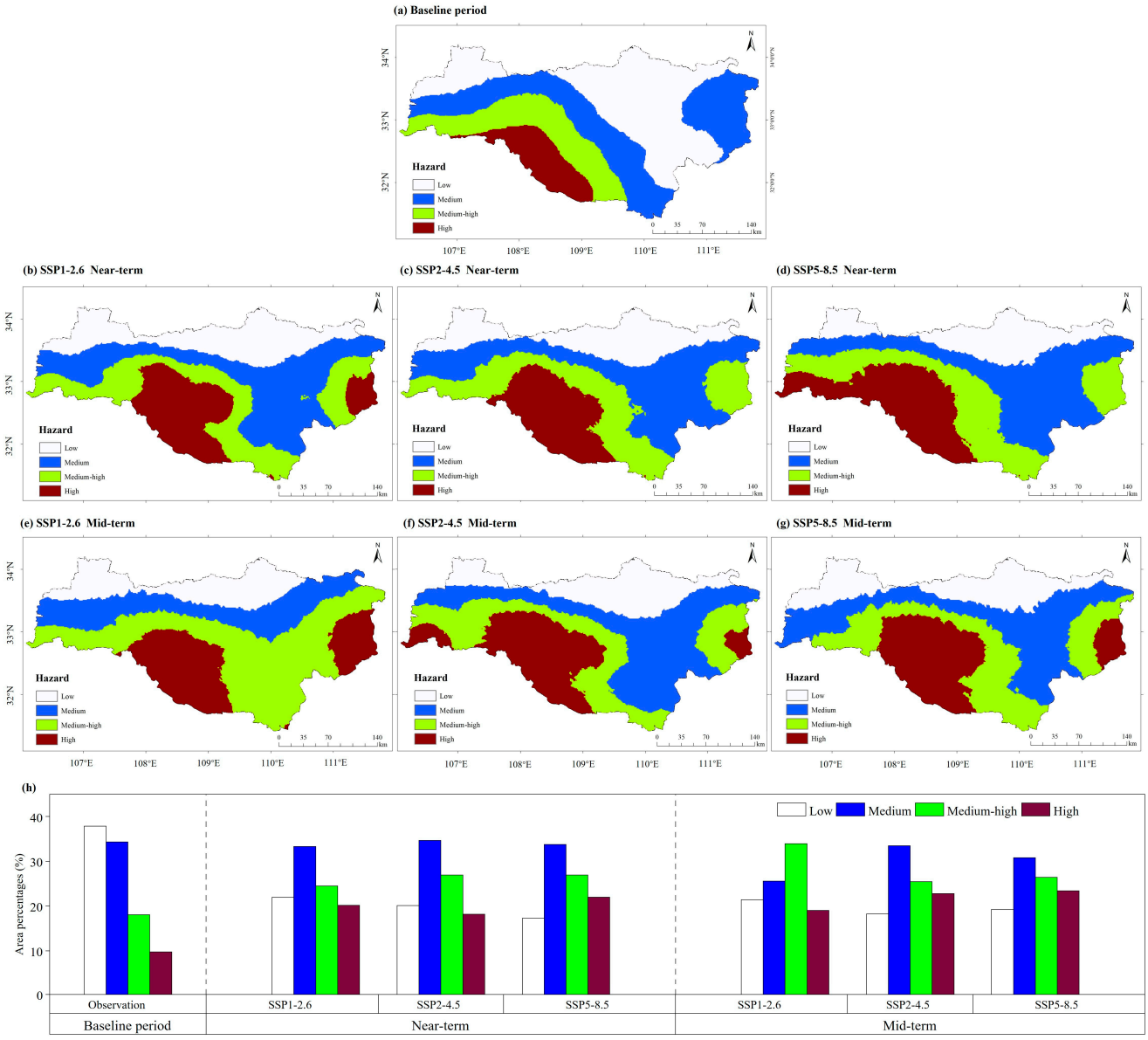

Figure 10. Spatial distributions (**a**–**g**) of hazard indicators and area percentages (**h**) of different hazard risk zones in the upper HRB during baseline period (1995–2014), near-term (2023–2042) and mid-term (2043–2062) under the three SSP-RCP scenarios.

3.4.2. Sensitivity Indicators

Figure 11 shows the maps of the sensitivity of the environment to flooding in the upper HRB during the baseline period (1995–2014), the near-term (2023–2042) and the mid-term (2043–2062) under the three SSP-RCP scenarios. It can be seen that the spatial patterns of environmental sensitivity exhibit consistency across different periods and under different scenarios. The areas of high sensitivity are predominantly located in the southwestern region of the basin, whereas the northern regions have lower sensitivity to flooding, which is similar to the spatial distributions of flood hazard. Figure 11 also shows the area percentages of different sensitivity zones across different periods and under different scenarios. The area percentages of high-, medium–high-, medium-, and low-sensitivity areas during the baseline period are 21.16%, 28.39%, 29.19%, and 21.02%, respectively. In the future near-term, the area percentage of high-sensitivity areas will be

the largest under the SSP1-2.6 scenario (22.47%), followed by the SSP5-8.5 scenario (21.57%), and will be the smallest under the SSP2-4.5 scenario (20.61%). In the future mid-term, the area percentage of high-sensitivity areas will be the largest under the SSP5-8.5 scenario (24.17%), followed by the SSP1-2.6 scenario (22.49%), and will be the smallest under the SSP2-4.5 scenario (20.32%). Under the SSP5-8.5 and SSP1-2.6 scenarios, the proportion of high-sensitivity areas will further increase during the future mid-term compared with that during the near-term. The high-sensitivity areas under the SSP2-4.5 scenario during the future near-term and mid-term will be lower than those during the baseline period.

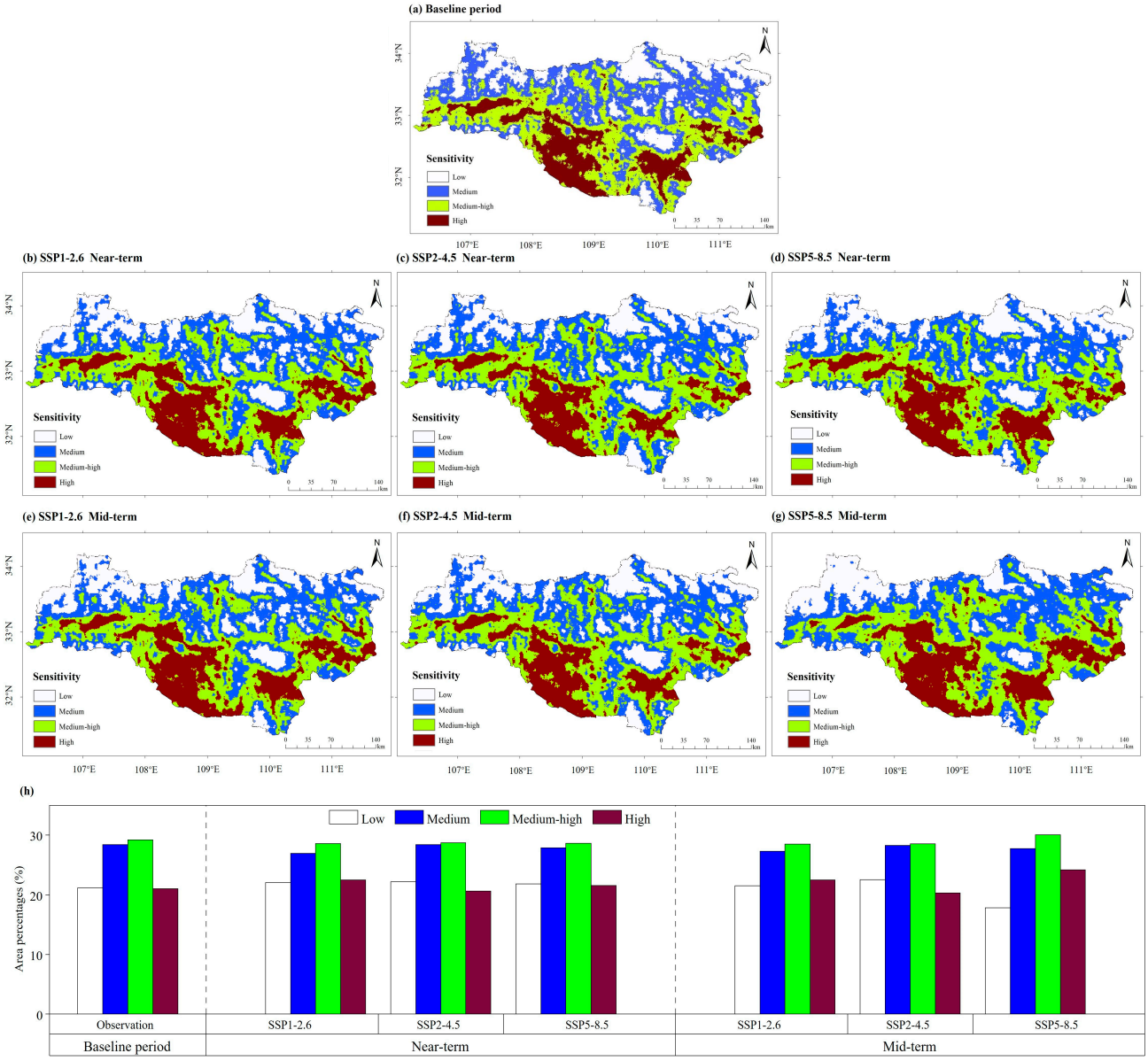

Figure 11. Spatial distributions (**a**–**g**) of sensitivity indicators and area percentages (**h**) of different sensitivity zones in the upper HRB during baseline period (1995–2014), near-term (2023–2042) and mid-term (2043–2062) under the three SSP-RCP scenarios.

3.4.3. Vulnerability Indicators

Figure 12 shows maps of the flood vulnerability in the upper HRB during the baseline period (1995–2014), the near-term (2023–2042) and the mid-term (2043–2062) under the three SSP-RCP scenarios. Overall, the regions characterized by high and medium–high vulnerability are predominantly located in the eastern and western regions of the basin,

where population density is concentrated. Figure 12 also shows the area percentages of different vulnerability zones under different scenarios during different periods. Relative to the baseline period, the proportions of high- and medium-vulnerability areas are projected to experience a significant increase in future periods, while the proportions of medium–high and low-vulnerability areas will decrease in future periods. Comparing different periods, the proportions of high-, medium–high, and medium-vulnerability areas in the near-term will be greater than in the mid-term under the same SSP-RCP scenario. In terms of different scenarios, the area percentages of high-, medium–high-, and medium-vulnerability areas during the same period under the SSP5-8.5 scenario will account for the largest proportion, followed by the SSP1-2.6 scenario, and the smallest will be seen under SSP2-4.5 the scenario. This is primarily due to the fact that SSP1 and SSP5 represent more optimistic socio-economic development scenarios, whereas SSP2 serves as a middle-ground pathway. The proportions of medium-, medium–high-, and high-vulnerability areas during the future near-term under the SSP5-8.5 scenario are projected to account for the largest proportions, at 35.58%, 18.59%, and 5.75%, respectively.

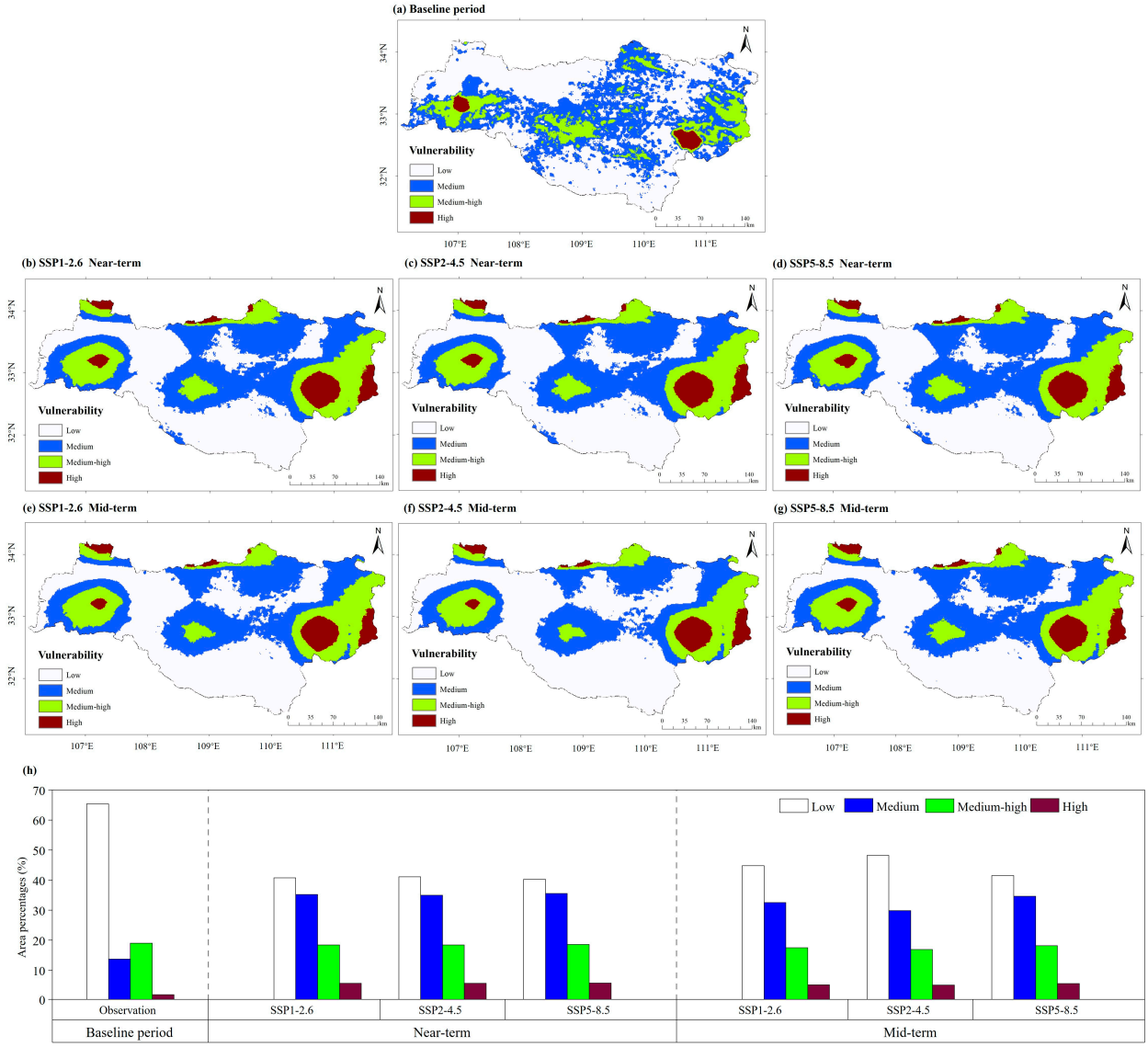

Figure 12. Spatial distributions (**a**–**g**) of vulnerability indicators and area percentages (**h**) of different vulnerability zones in the upper HRB during baseline period (1995–2014), near-term (2023–2042) and mid-term (2043–2062) under the three SSP-RCP scenarios.

3.4.4. Projection of Future Flood Risk

Figure 13 shows the maps of flood risk in the upper HRB during the baseline period (1995–2014), near-term (2023–2042) and mid-term (2043–2062) under the three SSP-RCP scenarios, which were obtained by integrating hazard, sensitivity, and vulnerability indicators using the entropy weight method and GIS environment. Overall, high-flood-risk zones in different scenarios and periods are predominantly situated in the southwestern region of the basin, while a secondary high-risk center is projected to develop near the Danjiangkou Reservoir in the eastern part of the basin during future near-term and mid-term. As Figure 13 shows, the risk level progressively diminishes from high-risk areas to their surrounding regions. Figure 13 also shows the area percentages of different flood risk zones under different scenarios during different periods. It is evident that the proportions of high-risk and medium–high-risk areas in the upper HRB are projected to increase significantly during the future periods relative to that during the baseline period. The proportion of high-flood-risk areas under the SSP5-8.5 scenario will be largest during future mid-term, at 24.02%. Comparing different periods, the proportion of high-risk areas under the same SSP-RCP scenario in the future mid-term is projected to surpass that in the future near-term. Comparing different scenarios, the proportion of high risk areas will be the highest under the SSP5-8.5 scenario, followed by the SSP1-2.6 scenario, and lowest in the SSP2-4.5 scenario.

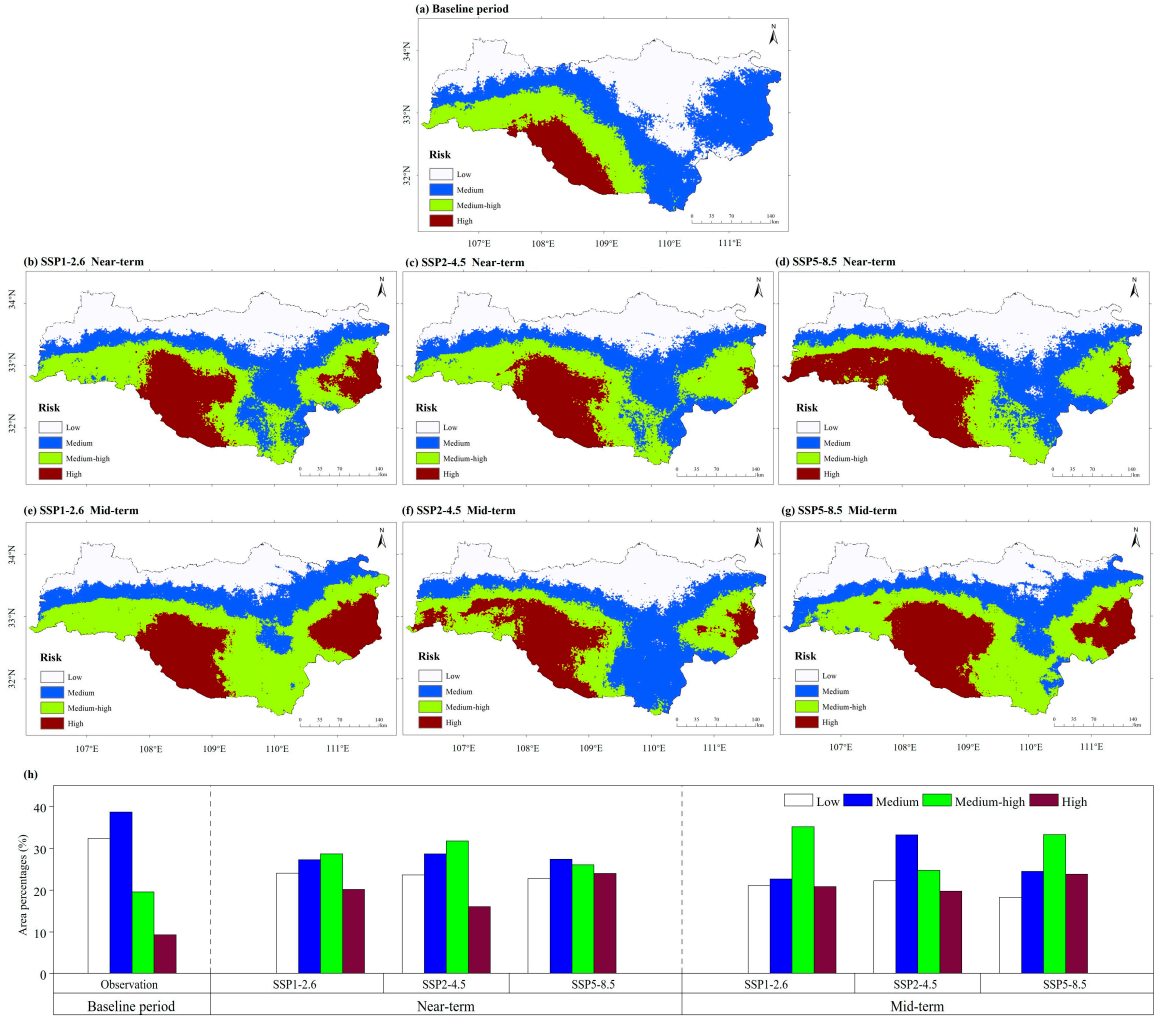

Figure 13. Spatial distributions (**a**–**g**) of flood risks and area percentage (**h**) of different flood risk zones in the upper HRB during baseline period (1995–2014), near-term (2023–2042) and mid-term (2043–2062) under the three SSP-RCP scenarios.

4. Discussion

The HRB, situated in the transitional zone between the northern and southern climates of China, is one of the areas that are most vulnerable to flooding disasters [48]. Forecasting precipitation, particularly extreme precipitation events, plays a crucial role in mitigating flood risks associated with such weather phenomena [47]. Therefore, this study used a statistical downscaling method combing EQM and four machine learning algorithms to bias-correct the GCM precipitation outputs, and applied six EPIs to define future precipitation extreme events in the HRB during the period of 2023–2100 under three SSP-RCP scenarios. The findings indicate that extreme precipitation is projected to exhibit increased instability in the future when compared to historical periods, and will show an increasing trend during 2023–2100 under the three scenarios, which is in agreement with the previous climate projection studies based on the CMIP5 under RCP2.6, RCP 4.5 and RCP 8.5 [78]. Regarding the spatial patterns of precipitation extremes, the high values of six EPIs during the periods of 1995–2014 and 2023–2100 are concentrated in the southeast and southwest of the HRB, which is also in line with other studies [49,54,78]. It is notable that the prediction of the spatio-temporal pattern of future extreme precipitation events is inseparable from the accuracy of future precipitation projection. However, the projection of future precipitation is influenced by various factors and has strong uncertainty, especially at the regional scale [65]. In general, the main sources of uncertainty in future precipitation projection include the uncertainty of GCMs selection, the uncertainty of natural variability inherent in the climate system, and the uncertainty of emission scenarios [79]. Therefore, more climate simulation models and superior downscaling methods need to be developed in future research.

Based on future precipitation and land use projections, the spatio-temporal evolution of runoff in the upper HRB was projected using DWM in this study. The results show that variability in runoff is strongly associated with variability in precipitation. Typically, a rising trend in precipitation results in a corresponding rise in runoff. However, the average annual runoff in the upper HRB reveals a decrease in the future, with the exception of that under the SSP5-8.5 scenario during the future mid-term, which is in line with the previous study [50]. The main reasons for the decrease in runoff in the upper HRB are the increasing temperature, the construction of water transfer projects, the operation of reservoirs and the influence of other human activities [50,80]. However, the forecast of future runoff is often uncertain due to the influence of various factors, such as uncertainties in hydrological models, uncertainties in climate scenarios, and uncertainties in land use predictions [81,82].

Utilizing projections of future precipitation and runoff, along with a grid dataset of GDP and POP under the SSP scenarios, a flood disaster assessment index system was established, and the entropy method was used to assess the hazard, sensitivity, vulnerability, and the comprehensive risk of flood disasters in the upper HRB during the future near-term (2023–2042) and the mid-term (2043–2062). The results show that the high-risk and medium–high-risk areas will expand further in the near-term (2023–2042) and mid-term (2043–2062), with more areas facing a higher flood risk. In the future, regions identified as high-risk will be situated in the southwestern and eastern areas of the upper HRB (Figure 13). Combining the spatial distribution of risk indicators (Figures S1–S6), these locations are characterized by flat terrain, proximity to rivers, high population density, concentrated property holdings and advanced economic development levels, and are also the center of high-frequency heavy rainfall. Furthermore, the land use types in these areas are mainly urban land and cultivated land. Under the combined effects of multiple factors, these areas exhibit a high level of hazard, sensitivity, and vulnerability, which can easily cause serious flood disasters losses. The northern region of the upper HRB presents the lowest flood risk, due to being far away from rivers and at a higher elevation. Moreover, the land types in these areas are mostly wood land, which is not in line with the needs of social-economic development and human life, presenting a sparse population and low social activity intensity. Therefore, these areas are not prone to causing serious flood losses.

There are some limitations in this study. In this study, extreme precipitation and land use in the HRB were projected. In terms of the projection and assessment of runoff and flood disaster risk, the focus was on the upper HRB. The middle and lower reaches of the watershed may be more susceptible to flood disaster. The runoff and flood disaster risk are not only affected by climate change, but also by human activities. The middle and lower reaches of the HRB are human settlement areas, which belong to regions with intense human activities. Large-scale water diversion projects, multi-level reservoir regulation, land use change, water withdrawal activities, water resources utilization, disaster prevention and mitigation measures and other human activities will have an impact on the projection of runoff and flood disaster risks. Due to the availability of these data, this study focuses on analyzing the runoff and flood disaster risk in the upper HRB. In the future, relevant information will be collected to conduct research on the projection of runoff and flood disaster risk in the middle and lower reaches of the HRB. In addition, projecting seasonal cycles of future extreme precipitation will help to more clearly examine the flood disaster risk. The periodic characteristics of extreme precipitation at the monthly and seasonal scales will be further explored, and the spatio-temporal response relationship between interannual fluctuations in extreme precipitation and flood disaster risk will also be discussed in a future study. Furthermore, it is essential to explore the physical mechanisms of future increases in flood disaster risk caused by extreme precipitation, which is important for decision makers to mitigate future flood disaster risk.

5. Conclusions

In this study, we explored the future spatio-temporal patterns of the extreme precipitation, runoff, and flood risk in the HRB during future periods under SSP1-2.6, SSP2-4.5, and SSP5-8.5 scenarios. The principal conclusions can be summarized as follows:

(1) The simulations of GCMs predict a consistent increase in intensity (Rx1day, Rx5day, PRCPTOT, SDII), frequency (R20m), and duration (CWD) of precipitation extremes over the HRB during the 21st century. The intensity and frequency of extreme precipitation events are projected to increase more significantly under higher-emission scenarios. The increases in Rx1day, Rx5day, PRCPTOT, SDII, R20 and CWD under the SSP5-8.5 scenario are 4.6 mm/10 a, 7.2 mm/10 a, 61.6 mm/10 a, 0.3 mm/day/10 a, 1 day/10 a and 0.2 day/10 a, respectively. The spatial distributions of precipitation intensity, frequency, and duration in future (2023–2100) are consistent with those in the baseline period (1995–2014). The mean values of precipitation intensity indices in future are higher than those in the baseline period;

(2) The changes in annual runoff over the upper HRB during period of 2023–2062 under three SSP-RCP scenarios will exhibit a nonsignificant upward trend over time in comparison with the baseline period. In the future near-term (2023–2042), the average annual runoff is projected to decline under the SSP1-2.6, SSP2-4.5, and SSP5-8.5 scenarios when compared to the baseline period, with amplitudes of −19.64%, −19.33%, and −6.63%, respectively. In the future mid-term (2043–2062), the average annual runoff will decrease under SSP1-2.6 and SSP2-4.5 scenarios, with amplitudes of −9.33% and −10.48%, respectively, while under the SSP5-8.5 scenario, it will show an increase, with an amplitude of 15.66%. The spatial patterns of average annual runoff depth in the upper HRB show a gradient-based decreasing trend from southwest to northeast;

(3) The high-flood-risk center in the future near-term (2023–2042) and mid-term (2043–2062) will be distributed in the southwestern region of the upper HRB, and a second high-flood-risk center will be formed near the Danjiangkou Reservoir in the eastern region of the basin. The proportions of high- and medium–high-flood-risk areas are projected to increase significantly in the future relative to those seen during the baseline period. The proportion of high-flood-risk areas in the future will be the highest under the SSP5-8.5 scenario, followed by the SSP1-2.6 scenario, and the lowest in the SSP2-4.5 scenario. The proportion of high-flood-risk areas under the SSP5-8.5 scenario will be the largest during the future mid-term, at 24.02%.

Supplementary Materials: The following supporting information can be downloaded at: https://www.mdpi.com/article/10.3390/rs16213980/s1, Table S1: List of the selected CMIP6 models; Figure S1: Spatial distribution of observed Rx1day, Rx5day, PRCPTOT, SDII, R20mm, and CWD based on CN05.1 in the upper HRB during baseline period (1995–2014); Figure S2: Spatial distribution of projected Rx1day, Rx5day in the upper HRB during near-term (2023–2042) and mid-term (2043–2062) under the three SSP-RCP scenarios; Figure S3: Spatial distribution of projected PRCPTOT, SDII in the upper HRB; Figure S4: Spatial distribution of projected R20mm, CWD in the upper HRB; Figure S5: Spatial distribution of GDP, POP, slope, and distance to river in the upper HRB; Figure S6: Spatial distribution of GDP, POP in the upper HRB.

Author Contributions: D.W.: conceptualization; data curation; formal analysis; investigation; methodology; validation; visualization; writing—original draft; writing—review and editing; funding acquisition. J.L.: conceptualization; formal analysis; funding acquisition; investigation; methodology; supervision; writing—review and editing. W.S.: formal analysis; funding acquisition; resources; writing—review and editing. H.S.: formal analysis; writing—review and editing. G.Z.: methodology; validation; visualization. X.F.: writing—review and editing. All authors have read and agreed to the published version of the manuscript.

Funding: This research was funded by the National Natural Science Foundation of China, grant number U2240223, the Innovation Foundation of Hebei University of Engineering, grant number SJ2401002179, the National Key Research and Development Program of China, grant number 2022YFC3090600, and the Key Science and Technology Program Project of the Ministry of Emergency Management of China, grant number 2024EMST020202.

Data Availability Statement: All data that support the findings of this study are included within the article and Supplementary Files.

Conflicts of Interest: The authors declare no conflicts of interest.

References

1. Trenberth, K. Changes in Precipitation with Climate Change. *Clim. Res.* **2011**, *47*, 123–138. [CrossRef]
2. Veiga, S.F.; Yuan, H. Performance-Based Projection of Precipitation Extremes over China Based on CMIP5/6 Models Using Integrated Quadratic Distance. *Weather Clim. Extrem.* **2021**, *34*, 100398. [CrossRef]
3. Myhre, G.; Alterskjær, K.; Stjern, C.W.; Hodnebrog, Ø.; Marelle, L.; Samset, B.H.; Sillmann, J.; Schaller, N.; Fischer, E.; Schulz, M.; et al. Frequency of Extreme Precipitation Increases Extensively with Event Rareness under Global Warming. *Sci. Rep.* **2019**, *9*, 16063. [CrossRef]
4. Mukherjee, S.; Aadhar, S.; Stone, D.; Mishra, V. Increase in Extreme Precipitation Events under Anthropogenic Warming in India. *Weather Clim. Extrem.* **2018**, *20*, 45–53. [CrossRef]
5. EM-DAT. EM-DAT Public 2021 [EB/OL]. Available online: https://www.emdat.be (accessed on 10 December 2023).
6. WMO. *Atlas of Mortality and Economic Losses from Weather, Climate and Water-Related Hazards 2021*; WMO: Geneva, Switzerland, 2021.
7. Yang, S.; Zhao, B.; Yang, D.; Wang, T.; Yang, Y.; Ma, T.; Santisirisomboon, J. Future Changes in Water Resources, Floods and Droughts under the Joint Impact of Climate and Land-Use Changes in the Chao Phraya Basin, Thailand. *J. Hydrol.* **2023**, *620*, 129454. [CrossRef]
8. Wang, L.; Li, Y.; Li, M.; Li, L.; Liu, F.; Liu, D.L.; Pulatov, B. Projection of Precipitation Extremes in China's Mainland Based on the Statistical Downscaled Data from 27 GCMs in CMIP6. *Atmos. Res.* **2022**, *280*, 106462. [CrossRef]
9. Luo, P.; Wang, X.; Zhang, L.; Mohd Arif Zainol, M.R.R.; Duan, W.; Hu, M.; Guo, B.; Zhang, Y.; Wang, Y.; Nover, D. Future Land Use and Flood Risk Assessment in the Guanzhong Plain, China: Scenario Analysis and the Impact of Climate Change. *Remote Sens.* **2023**, *15*, 5778. [CrossRef]
10. IPCC. *Climate Change 2021: The Physical Science Basis*; Cambridge University Press: Cambridge, UK, 2021.
11. Thackeray, C.W.; Hall, A.; Norris, J.; Chen, D. Constraining the Increased Frequency of Global Precipitation Extremes under Warming. *Nat. Clim. Chang.* **2022**, *12*, 441–448. [CrossRef]
12. Zhao, L.; Li, L.; Li, Y.; Yang, P.; Liu, X.; Zhou, Z.; Zhong, H.; Ding, Y. Global Extreme Precipitation Characteristics: The Perspective of Climate and Large River Basins. *Clim. Dyn.* **2024**, *62*, 1013–1030. [CrossRef]
13. Li, S.; Chen, Y.; Wei, W.; Fang, G.; Duan, W. The Increase in Extreme Precipitation and Its Proportion over Global Land. *J. Hydrol.* **2024**, *628*, 130456. [CrossRef]
14. Qin, P.; Xie, Z.; Zou, J.; Liu, S.; Chen, S. Future Precipitation Extremes in China under Climate Change and Their Physical Quantification Based on a Regional Climate Model and CMIP5 Model Simulations. *Adv. Atmos. Sci.* **2021**, *38*, 460–479. [CrossRef]
15. IPCC. *Climate Change 2022: Impacts, Adaptation, and Vulnerability*; Cambridge University Press: Cambridge, UK, 2022.
16. Wang, L.; Chen, S.; Zhu, W.; Ren, H.; Zhang, L.; Zhu, L. Spatiotemporal Variations of Extreme Precipitation and Its Potential Driving Factors in China's North-South Transition Zone during 1960–2017. *Atmos. Res.* **2021**, *252*, 105429. [CrossRef]

17. Sun, W.; Mu, X.; Song, X.; Wu, D.; Cheng, A.; Qiu, B. Changes in Extreme Temperature and Precipitation Events in the Loess Plateau (China) during 1960–2013 under Global Warming. *Atmos. Res.* **2016**, *168*, 33–48. [CrossRef]
18. Mondal, S.K.; Huang, J.; Wang, Y.; Su, B.; Kundzewicz, Z.W.; Jiang, S.; Zhai, J.; Chen, Z.; Jing, C.; Jiang, T. Changes in Extreme Precipitation across South Asia for Each 0.5 °C of Warming from 1.5 °C to 3.0 °C above Pre-Industrial Levels. *Atmos. Res.* **2022**, *266*, 105961. [CrossRef]
19. Li, Z.; Fang, H. Impacts of Climate Change on Water Erosion: A Review. *Earth-Sci. Rev.* **2016**, *163*, 94–117. [CrossRef]
20. Rojpratak, S.; Supharatid, S. Regional Extreme Precipitation Index: Evaluations and Projections from the Multi-Model Ensemble CMIP5 over Thailand. *Weather Clim. Extrem.* **2022**, *37*, 100475. [CrossRef]
21. Eyring, V.; Bony, S.; Meehl, G.A.; Senior, C.A.; Stevens, B.; Stouffer, R.J.; Taylor, K.E. Overview of the Coupled Model Intercomparison Project Phase 6 (CMIP6) Experimental Design and Organization. *Geosci. Model Dev.* **2016**, *9*, 1937–1958. [CrossRef]
22. O'Neill, B.C.; Kriegler, E.; Riahi, K.; Ebi, K.L.; Hallegatte, S.; Carter, T.R.; Mathur, R.; van Vuuren, D.P. A New Scenario Framework for Climate Change Research: The Concept of Shared Socioeconomic Pathways. *Clim. Chang.* **2013**, *122*, 387–400. [CrossRef]
23. Patel, J.; Gnanaseelan, C.; Chowdary, J.S.; Parekh, A. A Quantile Mapping Approach-based Bias Correction in Coupled Model Intercomparison Project Phase 5 Models for Decadal Temperature Predictions over India. *Int. J. Climatol.* **2021**, *42*, 2455–2469. [CrossRef]
24. Tong, Y.; Gao, X.; Han, Z.; Xu, Y.; Xu, Y.; Giorgi, F. Bias Correction of Temperature and Precipitation over China for RCM Simulations Using the QM and QDM Methods. *Clim. Dyn.* **2020**, *57*, 1425–1443. [CrossRef]
25. Jose, D.M.; Vincent, A.M.; Dwarakish, G.S. Improving Multiple Model Ensemble Predictions of Daily Precipitation and Temperature through Machine Learning Techniques. *Sci. Rep.* **2022**, *12*, 4678. [CrossRef] [PubMed]
26. Ahmed, K.; Sachindra, D.A.; Shahid, S.; Iqbal, Z.; Nawaz, N.; Khan, N. Multi-Model Ensemble Predictions of Precipitation and Temperature Using Machine Learning Algorithms. *Atmos. Res.* **2020**, *236*, 104806. [CrossRef]
27. Yu, Y.; Mao, J.; Wullschleger, S.D.; Chen, A.; Shi, X.; Wang, Y.; Hoffman, F.M.; Zhang, Y.; Pierce, E. Machine Learning-Based Observation-Constrained Projections Reveal Elevated Global Socioeconomic Risks from Wildfire. *Nat. Commun.* **2022**, *13*, 1250. [CrossRef]
28. Liang, X.; Guan, Q.; Clarke, K.C.; Liu, S.; Wang, B.; Yao, Y. Understanding the Drivers of Sustainable Land Expansion Using a Patch-Generating Land Use Simulation (PLUS) Model: A Case Study in Wuhan, China. *Comput. Environ. Urban Syst.* **2021**, *85*, 101569. [CrossRef]
29. Liang, X.; Liu, X.; Chen, G.; Leng, J.; Wen, Y.; Chen, G. Coupling Fuzzy Clustering and Cellular Automata Based on Local Maxima of Development Potential to Model Urban Emergence and Expansion in Economic Development Zones. *Int. J. Geogr. Inf. Sci.* **2020**, *34*, 1–23. [CrossRef]
30. Song, Y.H.; Chung, E.-S.; Shahid, S. Differences in Extremes and Uncertainties in Future Runoff Simulations Using SWAT and LSTM for SSP Scenarios. *Sci. Total Environ.* **2022**, *838*, 156162. [CrossRef] [PubMed]
31. Chang, J.; Zhang, H.; Wang, Y.; Zhang, L. Impact of Climate Change on Runoff and Uncertainty Analysis. *Nat. Hazards* **2017**, *88*, 1113–1131. [CrossRef]
32. Ji, H.; Peng, D.; Gu, Y.; Luo, X.; Pang, B.; Zhu, Z. Snowmelt Runoff in the Yarlung Zangbo River Basin and Runoff Change in the Future. *Remote Sens.* **2022**, *15*, 55. [CrossRef]
33. Shi, L.; Feng, P.; Wang, B.; Liu, D.L.; Zhang, H.; Liu, J.; Yu, Q. Assessing Future Runoff Changes with Different Potential Evapotranspiration Inputs Based on Multi-Model Ensemble of CMIP5 Projections. *J. Hydrol.* **2022**, *612*, 128042. [CrossRef]
34. Shi, H.; Chen, J.; Li, T.; Wang, G. A New Method for Estimation of Spatially Distributed Rainfall through Merging Satellite Observations, Raingauge Records, and Terrain Digital Elevation Model Data. *J. Hydro-Environ. Res.* **2020**, *28*, 1–14. [CrossRef]
35. Zhang, A.; Shi, H.; Li, T.; Fu, X. Analysis of the Influence of Rainfall Spatial Uncertainty on Hydrological Simulations Using the Bootstrap Method. *Atmosphere* **2018**, *9*, 71. [CrossRef]
36. Chen, J.; Xia, J.; Li, T.; Wang, M. Application of Digital River Basin Model to Long River Basin of Upper Yangtze. *J. Hydroelectr. Eng.* **2019**, *38*, 1–10. (In Chinese) [CrossRef]
37. Wang, H.; Liu, J.; Liu, X.; Wang, D. Construction of DYRIM of Qinghai Lake Basin Based on ANUSPLIN. *Water Resour. Prot.* **2024**, *40*, 82–91. (In Chinese) [CrossRef]
38. Xue, Y.; Qin, C.; Wu, B.; Zhang, G.; Fu, X.; Ma, H.; Li, D.; Wang, B. Simulation of Runoff Process Based on the 3-D River Network. *J. Hydrol.* **2023**, *626*, 130192. [CrossRef]
39. Shi, H.; Li, T.; Wang, K.; Zhang, A.; Wang, G.; Fu, X. Physically Based Simulation of the Streamflow Decrease Caused by Sediment-trapping Dams in the Middle Yellow River. *Hydrol. Process.* **2016**, *30*, 783–794. [CrossRef]
40. Wang, Z.; Xu, M.; Liu, X.; Singh, D.K.; Fu, X. Quantifying the Impact of Climate Change and Anthropogenic Activities on Runoff and Sediment Load Reduction in a Typical Loess Plateau Watershed. *J. Hydrol. Reg. Stud.* **2022**, *39*, 100992. [CrossRef]
41. Shi, H.; Li, T. Estimating Hydrological Parameters Based on Rainfall Patterns in River Basins with No Long-Term Historical Observations. *J. Hydrol.* **2017**, *553*, 651–661. [CrossRef]
42. Li, G.; Liu, J.; Shao, W. Research Progress in Flood Disaster Risk Assessment and Zoning. *J. China Hydrol.* **2023**, *43*, 15–20. (In Chinese) [CrossRef]
43. Wang, Y.; Zhai, J.; Gao, G.; Liu, Q.; Song, L. Risk Assessment of Rainstorm Disasters in the Guangdong–Hong Kong–Macao Greater Bay Area of China during 1990–2018. *Geomat. Nat. Hazards Risk* **2022**, *13*, 267–288. [CrossRef]

44. Chen, Y.; Alexander, D. Integrated Flood Risk Assessment of River Basins: Application in the Dadu River Basin, China. *J. Hydrol.* **2022**, *613*, 128456. [CrossRef]
45. Shi, Y.; Zhai, G.; Zhou, S.; Lu, Y.; Chen, W.; Deng, J. How Can Cities Respond to Flood Disaster Risks under Multi-Scenario Simulation? A Case Study of Xiamen, China. *Int. J. Environ. Res. Public Health* **2019**, *16*, 618. [CrossRef]
46. Mitra, R.; Das, J. A Comparative Assessment of Flood Susceptibility Modelling of GIS-Based TOPSIS, VIKOR, and EDAS Techniques in the Sub-Himalayan Foothills Region of Eastern India. *Environ. Sci Pollut Res* **2023**, *30*, 16036–16067. [CrossRef]
47. Deng, P.; Zhang, M.; Hu, Q.; Wang, L.; Bing, J. Pattern of Spatio-Temporal Variability of Extreme Precipitation and Flood-Waterlogging Process in Hanjiang River Basin. *Atmos. Res.* **2022**, *276*, 106258. [CrossRef]
48. Jin, H.; Chen, X.; Zhong, R.; Liu, M.; Ye, C. Construction of Precipitation Index Based on Ensemble Forecast and Heavy Precipitation Forecast in the Hanjiang River Basin, China. *Atmos. Res.* **2023**, *287*, 106701. [CrossRef]
49. Hao, W.; Hao, Z.; Yuan, F.; Ju, Q.; Hao, J. Regional Frequency Analysis of Precipitation Extremes and Its Spatio-Temporal Patterns in the Hanjiang River Basin, China. *Atmosphere* **2019**, *10*, 130. [CrossRef]
50. Zhou, X.; Chen, W.; Liu, Q.; Shen, H.; Cai, S.; Lei, X. Future Runoff Forecast in Hanjiang River Basin Based on Wetspa Model and CMIP6 Model. *Front. Environ. Sci.* **2022**, *10*, 980949. [CrossRef]
51. Jin, H.; Chen, X.; Zhong, R.; Wu, P.; Li, D. Spatio-Temporal Changes of Precipitation in the Hanjiang River Basin under Climate Change. *Theor. Appl. Clim.* **2021**, *146*, 1441–1458. [CrossRef]
52. Wang, D.; Liu, J.; Luan, Q.; Shao, W.; Fu, X.; Wang, H.; Gu, Y. Projection of Future Precipitation Change Using CMIP6 Multimodel Ensemble Based on Fusion of Multiple Machine Learning Algorithms: A Case in Hanjiang River Basin, China. *Meteorol. Appl.* **2023**, *30*, e2144. [CrossRef]
53. Hao, W.; Shao, Q.; Wei, P.; Zhu, C.; Chen, X.; Chen, R. Evaluation and Projection of the Annual Maximum Streamflow in Response to Anthropogenic and Climatic Effects under Nonstationary Conditions in the Hanjiang River Basin, China. *J. Water Clim. Chang.* **2022**, *13*, 1855–1877. [CrossRef]
54. Qin, Z.; Peng, T.; Singh, V.P.; Chen, M. Spatio-Temporal Variations of Precipitation Extremes in Hanjiang River Basin, China, during 1960–2015. *Theor. Appl. Climatol.* **2019**, *138*, 1767–1783. [CrossRef]
55. Rudke, A.P.; Fujita, T.; de Almeida, D.S.; Eiras, M.M.; Xavier, A.C.F.; Rafee, S.A.A.; Santos, E.B.; de Morais, M.V.B.; Martins, L.D.; de Souza, R.V.A.; et al. Land Cover Data of Upper Parana River Basin, South America, at High Spatial Resolution. *Int. J. Appl. Earth Obs. Geoinf.* **2019**, *83*, 101926. [CrossRef]
56. Shi, J.; Li, X. Simulation of Runoff at Different Time Scales in Dianchi Watershed Based on SWAT Model. *Water Resour. Power* **2022**, *40*, 37–40. (In Chinese) [CrossRef]
57. Liang, S.; Cheng, J.; Jia, K.; Jiang, B.; Zhou, J. The Global Land Surface Satellite (GLASS) Product Suite. *Bull. Am. Meteorol. Soc.* **2021**, *102*, E323–E337. [CrossRef]
58. Xu, B.; Li, J.; Park, T.; Liu, Q.; Zeng, Y.; Yin, G.; Zhao, J.; Fan, W.; Yang, L.; Knyazikhin, Y.; et al. An Integrated Method for Validating Long-Term Leaf Area Index Products Using Global Networks of Site-Based Measurements. *Remote Sens. Environ.* **2018**, *209*, 134–151. [CrossRef]
59. Wu, J.; Gao, X. A Gridded Daily Observation Dataset over China Region and Comparison with the Other Dataset. *Chin. J. Geophys.* **2013**, *56*, 1102–1111. (In Chinese) [CrossRef]
60. Luo, Y.; Xu, C.; Chu, Z.; Sun, Q.; Chen, L. Application of CN05.1 meteorological data in watershed hydrological simulation: A case study in the upper reaches of Kaidu River basin. *Clim. Chang. Res.* **2020**, *16*, 287–295. (In Chinese) [CrossRef]
61. Wang, D.; Wang, A. Applicability Assessment of GPCC and CRU Precipitation Products in China during 1901 to 2013. *Clim. Environ. Res.* **2017**, *22*, 446–462. (In Chinese) [CrossRef]
62. Wang, D.; Liu, J.; Wang, H.; Shao, W.; Mei, C.; Ding, X. Performance Evaluations of CMIP6 and CMIP5 Models for Precipitation Simulation over the Hanjiang River Basin, China. *J. Water Clim. Chang.* **2022**, *13*, 2089–2106. [CrossRef]
63. Chen, L.; Xu, C.; Li, X. Projections of Temperature Extremes Based on Preferred CMIP5 Models: A Case Study in the Kaidu-Kongqi River Basin in Northwest China. *J. Arid Land* **2021**, *13*, 568–580. [CrossRef]
64. Wang, Y.; Li, X.; Liu, S.; Han, Z.; Song, L.; Ke, Z.; Chen, K. Climate Services for Water Resource Management in China: The Case Study of Danjiangkou Reservoir. *J. Meteorol. Res.* **2021**, *35*, 87–100. [CrossRef]
65. Yue, Y.; Yan, D.; Yue, Q.; Ji, G.; Wang, Z. Future Changes in Precipitation and Temperature over the Yangtze River Basin in China Based on CMIP6 GCMs. *Atmos. Res.* **2021**, *264*, 105828. [CrossRef]
66. Zhu, H.; Jiang, Z.; Li, J.; Li, W.; Sun, C.; Li, L. Does CMIP6 Inspire More Confidence in Simulating Climate Extremes over China? *Adv. Atmos. Sci.* **2020**, *37*, 1119–1132. [CrossRef]
67. Liao, W.; Liu, X.; Xu, X.; Chen, G.; Liang, X.; Zhang, H.; Li, X. Projections of Land Use Changes under the Plant Functional Type Classification in Different SSP-RCP Scenarios in China. *Sci. Bull.* **2020**, *65*, 1935–1947. [CrossRef]
68. Shao, W.; Su, X.; Lu, J.; Liu, J.; Yang, Z.; Mei, C.; Liu, C.; Lu, J. Urban Resilience of Shenzhen City under Climate Change. *Atmosphere* **2021**, *12*, 537. [CrossRef]
69. Wu, C.; Chen, B.; Huang, X.; Wei, Y. Effect of Land-Use Change and Optimization on the Ecosystem Service Values of Jiangsu Province, China. *Ecol. Indic.* **2020**, *117*, 106507. [CrossRef]
70. Pontlus, R.G. Quantification Error Versus Location Error in Comparison of Categorical Maps. *Photogramm. Eng. Remote Sens.* **2000**, *66*, 1011–1016. [CrossRef]

71. Liu, J.; Wang, G.; Li, H.; Gong, J.; Han, J. Water and Sediment Evolution in Areas with High and Coarse Sediment Yield of the Loess Plateau. *Int. J. Sediment Res.* **2013**, *28*, 448–457. [CrossRef]
72. Liu, J.; Wang, G.; Li, T.; Xue, H.; He, L. Sediment Yield Computation of the Sandy and Gritty Area Based on the Digital Watershed Model. *Sci. China Ser. E* **2006**, *49*, 752–763. [CrossRef]
73. Wang, G.; Wu, B.; Li, T. Digital Yellow River Model. *J. Hydro-Environ. Res.* **2007**, *1*, 1–11. [CrossRef]
74. Wang, C.; Wang, B.; Wang, Y.; Wang, Y.; Zhang, W. Improved Interrill Erosion Prediction by Considering the Impact of the Near-Surface Hydraulic Gradient. *Soil Tillage Res.* **2020**, *203*, 104687. [CrossRef]
75. Hu, L.; Zhang, Q.; Singh, V.; Wang, G.; He, C.; Zhao, J. Escalating Rainstorm-Induced Flood Risks in the Yellow River Basin, China. *Environ. Res. Lett.* **2024**, *19*, 064006. [CrossRef]
76. Li, S.; Wang, Z.; Lai, C.; Lin, C. Quantitative Assessment of the Relative Impacts of Climate Change and Human Activity on Flood Susceptibility Based on a Cloud Model. *J. Hydrol.* **2020**, *588*, 125051. [CrossRef]
77. Jiang, T.; Su, B.; Jing, C.; Wang, L. National and Provincial Population and Economy Projection Databases Under Shared Socioeconomic Pathways(SSP1-5)_v2[DS/OL]. V4. Science Data Bank. 2024. Available online: https://cstr.cn/31253.11.sciencedb.01683 (accessed on 10 July 2024).
78. Zhang, Q.M.; Wang, R.; Jiang, T.; Chen, S. Projection of Extreme Precipitation in the Hanjiang River Basin under Different RCP Scenarios. *Clim. Chang. Res.* **2020**, *16*, 276–286. (In Chinese) [CrossRef]
79. Duan, Q.; Xia, J.; Miao, C.; Sun, Q. The Uncertainty in Climate Change Projections by Global Climate Models. *Chin. J. Nat.* **2016**, *38*, 182–188. (In Chinese) [CrossRef]
80. Yaghmaei, H.; Sadeghi, S.; Moradi, H.; Gholamalifard, M. Effect of Dam Operation on Monthly and Annual Trends of Flow Discharge in the Qom Rood Watershed, Iran. *J. Hydrol.* **2018**, *557*, 254–264. [CrossRef]
81. Hou, Y.; Guo, H.; Yang, Y.; Liu, W. Global Evaluation of Runoff Simulation From Climate, Hydrological and Land Surface Models. *Water Resour. Res.* **2023**, *59*, e2021WR031817. [CrossRef]
82. Zhang, L.; Zhao, Z.; Wang, H.; Yang, Y.; Li, X. Discussion on Several Issues of Uncertainty in Hydrological Simulation under Climate Change. *Water Resour. Prot.* **2023**, *39*, 109–118. (In Chinese) [CrossRef]